ELECTROCHEMICAL POLARIZATION BEHAVIOUR OF Mg-Al ALLOYS IN NEAR-NEUTRAL SOLUTIONS

BY

YANING HU, B. Eng

A Thesis

Submitted to the School of Graduate Studies

In Partial Fulfillment of the Requirements

For the Degree

Master of Science

McMaster University

MASTER OF SCIENCE (2012) McMaster University

(Materials Science & Engineering) Hamilton Ontario

TITLE: ELECTROCHEMICAL POLARIZATION BEHAVIOUR OF Mg-Al ALLOYS IN NEAR-NEUTRAL SOLUTIONS

AUTHOR: Yaning Hu, B.Eng (Central South University)

SUPERVISORS: Professor Joseph R. McDermid,

Professor Joseph R. Kish,

Dr. Wenyue Zheng (CanmetMATERIALS)

NUMBER OF PAGES: xiii, 101

Abstract

A study has been conducted in mildly aggressive saline solutions to indentify subtle yet important difference in the anodic and cathodic process of three Mg-Al alloys, AZ31B, AM30 and AM60B in a partially passive state and a localized corrosion state. The influence of metallurgical factors and environment variables on the corrosion resistance and surface film breakdown process has been investigated using potentiodynamic and potentiostatic tests combined with optical microscopy.

All three Mg-Al alloys corroded in a partially protected state under open circuit conditions in the test solution and the surface film formed on each exhibited a similar breakdown potential. This indicates that metallurgical factors such as alloying additions and the presence of the β-phase ($Mg_{17}Al_{12}$) did not significantly influence the surface film breakdown process. AM60B exhibited improved corrosion resistance at potentials below the breakdown potential due to the formation of a more protective surface film. The β-phase, however, did not strongly influence either the anodic process at potentials above the breakdown potential or the cathodic process. It was determined that increasing the alloy Al content increases the corrosion potential of Mg-Al alloys, but also increases the risk of localized corrosion. The similar anodic and cathodic polarization behaviour exhibited by AZ31B and AM30 indicates that a 1 wt % Zn alloying addition does not strongly influence the corrosion resistance of these alloys. The die-cast skin of AM60B exhibited better corrosion resistance than the interior at potentials below the breakdown

potential due to the higher fraction of Al-rich β-phase, which improved the protective ability of the surface film. The semi-continuous β-phase network did not provide a strong micro-galvanic activity to drive anodic dissolution of the α-phase, therefore, did not significantly affect the corrosion resistance above the breakdown potential. The crystallographic texture exhibited by the extruded AM30 did not strongly affect the short-term and long-term corrosion resistance. AM30 showed a relatively steady passive state during long time exposures in a room temperature 0.01 M NaCl solution.

Acknowledgments

I would like to express my deepest gratitude to my supervisors, Dr. Joseph R. McDermid and Dr. Joseph R. Kish at McMaster University. Their assistance, encouragement and knowledgeable advice were a great aid throughout this work.

This gratitude is also expressed to Dr. Wenyue Zheng, who served as co-supervisor in CanmetMATERIALS (CMAT), for his invaluable discussion and instructive advice and great help.

I wish to thank the technical staff in Department of Material Science and Engineering, Mr. Doug Culley, Mr. Ed McCaffery and Mr. John Rodda, for their great help on my experiments. And I am also grateful to Dr. James Britten of the McMaster Analytical X-Ray Diffraction Facility (MAX) for providing XRD texture analysis.

I would like to thank my colleagues, Jennifer Thuss, Mehdi Taheri, Stephen Jones, Ryan Phillips, Jacek Dabrowski, and Aniruddho Pal for their helpful advice and assistance throughout my project.

I would like to show my gratitude to my friends at McMaster, Michael Nemcko, Felicia Arnor, for their valuable discussion and great help.

Very special thanks must be given to my family and my best friend, Jianhong Zhu. This thesis would not have been possible without their always support and encouragement.

Finally, I gratefully acknowledge the financial support from McMaster University and CanmetMATERIALS.

Table of Content

List of Figures

List of Tables

Chapter 1. Introduction

The North American 2020 strategic goal is to substitute 630 lbs of steel and aluminum for 340 lbs of magnesium automotive parts [1]. The Magnesium Front End Research and Development (MFERD) project is one of the major international efforts to bring together scientific and engineering expertise from Canada, China, and the United States in the field of magnesium technology [2]. The objectives of this project are to develop some key technologies and build a knowledge base for Mg applications. In this project, three commonly used magnesium alloys; rolled AZ31B, extruded AM30 and high pressure die cast AM60B were chosen for the new front end prototype design. One of the major factors limiting their application in the automotive industry is their poor corrosion resistance in near neutral saline environments, which correspond to typical road conditions.

Mg-Al alloys exposed to air and mildly aggressive solution are covered by a relatively protective surface film [3-20]. The stability of the film and corrosion resistance of Mg alloys is primarily related to their chemical composition, microstructure and the environment. The influence of these factors on the corrosion mechanisms of Mg alloys is not well defined and understood because these mechanisms are significantly different before and after the breakdown of the film. Some standard corrosion test solutions, such as 3~5 wt % NaCl solution, have been commonly employed to study the corrosion resistance of Mg alloys, in which Mg alloys suffer severe localized corrosion and exhibit extremely high corrosion rates [3, 8, 13, 21-31]. Obviously, a mildly aggressive corrosion

environment is more suitable for Mg alloy corrosion research to indentify the subtle yet important difference in corrosion behaviour for automotive use.

In this research, electrochemical techniques and optical microscopy were employed to examine the corrosion resistance of rolled AZ31B, extruded AM30 and die-cast AM60B in a mildly aggressive near-neutral saline solution (GM9540P) to better understand the critical metallurgical factors that control the corrosion and surface film breakdown processes. Key parameters investigated include the role of alloying elements (primarily Al and Zn), the presence of the β-phase ($Mg_{17}Al_{12}$), microstructural skin effect and applied potential. In addition, the influence of crystallographic texture and pre-exposure time on corrosion resistance of extruded AM30 has been studied using a 0.01 M NaCl solution. The information obtained from electrochemical testing in these solutions will greatly help to understand the corrosion resistance in commonly encountered environmental conditions.

Chapter 2. Literature Review

Mg-Al-Mn alloys with Zn are defined as the AZxx series, whereas Mg-Al-Mn alloys without Zn are defined as the AMxx series. For AZ31 and AM60 alloys series, the difference of chemical composition is minor [32]. The chemical composition limits for AZ31B, AM60B are listed in Table 2.1 according to ASTM standard [32]. It is should be noted that AM30 is a recently developed alloy, which mainly contains 3 wt % Al and 0.4 wt % Mn [33]. There has not been an ASTM standard specifying the chemical composition limits for AM30 so far. The major difference of chemical composition between these three alloys is AM60B has about 3 wt % higher Al content than that in AZ31B and AM30 and the presence of 1 wt % Zn in AZ31B only. It is also noted that the concentration of Fe in each is well below the 170 ppm (0.017 wt %) tolerance limit [34]. This indicates that commercial alloys have sufficient control of impurity level to optimize corrosion resistance. Thus, the poison elements, such as Fe, are unlikely to play a controlling role in the corrosion processes of the MFERD alloys.

Table 2.1 Chemical Composition of Experimental Alloys (wt %) [32-33].

Alloy	**Al**	**Zn**	**Mn**	**Fe**	**Si**	**Mg**
AZ31B	2.5-3.5	0.6-1.4	0.2-1.0	0.005	0.10	Balance
AM60B	5.5-6.5	0.22	0.24-0.6	0.005	0.1	Balance
AM30	3	N/A	0.4	N/A	N/A	Balance

AZ31 and AM30 are both single phase alloys [35]. HDPC die-cast AM60 has a dual-phase microstructure, in which the secondary β-phase ($Mg_{17}Al_{12}$) is precipitated on the grain boundaries. The precipitation of the β-phase from solid solution can be continuous or discontinuous [32]. The completed divorced morphology of the α/β eutectic has been reported in die-cast AM60 [36-37]. The small α-matrix grains have an almost spherical shape divided by small β-phase particles, which locate on the grain boundaries. Barbagallo et al. [36] reported that the Al concentration can vary from 2.5 wt % in the center of grain to about 10 wt % close to gain boundary region. By contrast, the Al concentration in β-phase is roughly constant at around 44 wt % [38]. High pressure die-cast skin has been wildly reported [21, 37, 39-40]. It has a finer grain size, higher fraction of β-phase than that in the interior. In these three alloys, Al-Mn intermetallic particles are randomly distributed in the grains and on the grain boundaries. Most Al-Mn intermetallic particles contain 0~2.5 wt % Fe to form various $Al_xMn_yFe_z$ with highly irregular shape and the average dimension of the Al-Mn particles is about 300 nm [31-32].

The corrosion resistance of Mg-Al alloys in saline environments is strongly influenced by the alloy composition, microstructure and the stability of a partially-protective surface film. Controlling factors include (i) composition of the solid solution α-matrix [25], (ii) presence of Al-Mn intermetallic particles [41-43], and (iii) the presence of the secondary β-phase [21, 24, 41, 44]. However, the extent to which each of these influences corrosion depends on whether corrosion is occurring above or below the apparent breakdown potential (E_b). This critical potential, E_b, is defined as a potential where the anodic current

density dramatically increases due to the breakdown of the surface film. The example is given in Figure 2.2.

2.1 Corrosion States of Mg-Al Alloys

Wang et al. [19] reported that AZxx alloys can exhibit passive behaviour in near-neutral saline solutions due to a partially protective film formed on the surface. They constructed a corrosion map for AZ31 and AZ91 as a function of electrode potential and ion concentration based on electrochemical measurements, as shown in Figure 2.1. The critical potential, V_c, acts as the boundary between the passivation and corrosion zone. This potential, which was determined by potentiostatic polarization tests, indicates the initiation of pits and accelerated localized corrosion. According to the corrosion map, both AZ31 and AZ91 can exhibit passive behaviour in various dilute solutions in the presence of aggressive anions, such as Cl^-, due to the location of the open circuit potential, E_{OCP} (or corrosion potential, E_{corr}), in the passivation zone. The Cl^- concentration limit for which E_{OCP} values lie within the passivation zone are 0.2 mol/L for AZ31 and 0.5 mol/L for AZ91. This indicates that an increase in alloyed Al content can extent the passivation zone to higher potentials for Mg-Al alloys.

From Figure 2.2, an increase in the concentration of Cl^- has no significant influence on the cathodic polarization behaviour. In contrast, the anodic polarization behaviour is strongly affected by the concentration of Cl^-. Mg-Al alloys only exhibits an apparent E_b in the anodic branch in dilute solution. Increasing the Cl^- concentration decreases E_b, which

effectively decreases the size of the passivation zone [19]. Thus, it is obvious that the presence of aggressive anion (Cl^-) and its concentration play a critical role affecting the corrosion state of Mg-Al alloys.

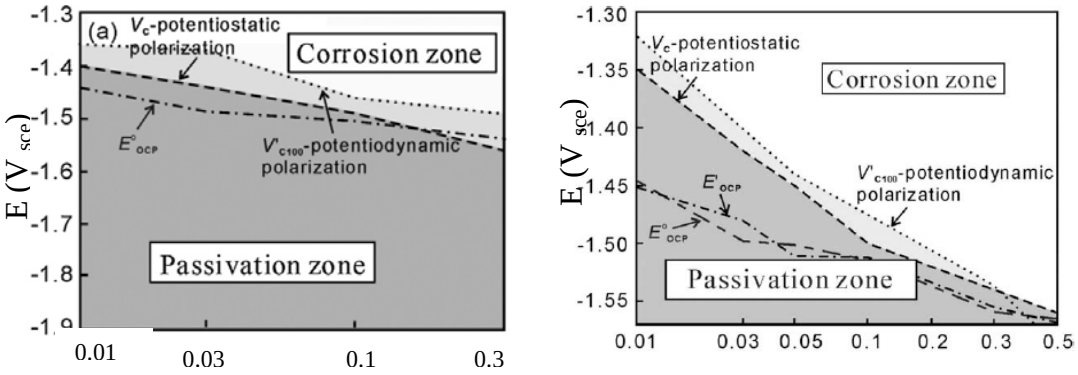

(a) AZ31 (b) AZ91

Figure 2.1 Corrosion maps for AZ31 and AZ91 alloy in NaCl solution [19].

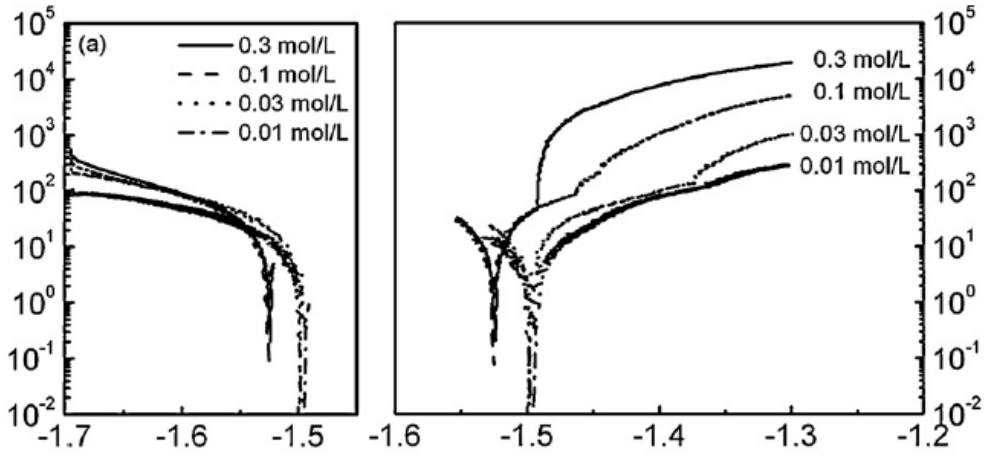

Figure 2.2 Cathodic and anodic polarization curves for AZ31 in various concentrated NaCl solutions [19].

Wang et al. [18] also compared the current density transient for AZ31 and AZ91 in corrosion zone (-1.30 V_{SCE}) and passivation zone (-1.50 V_{SCE}), respectively, when exposed in 0.01 M NaCl solution, as shown in Figure 2.3. It should be noted that -1.50 V_{SCE} is below E_{corr} based on the corrosion map (Figure 2.1) for both AZ31 and AZ91. This indicates that both alloys exhibit cathodic polarization at -1.50 V_{SCE}. Both AZ31 and AZ91 exhibited a remarkable higher current density in the corrosion state (Figure 2.3(a)) than that in the passivation state (Figure 2.3(b)). There was no significant difference between the steady-state current density observed on AZ31 and AZ91 in the passivation state, whereas a slightly different, but within one order of magnitude, steady-state current density was observed in the corrosion state. Tunold et al. [45] compared the corrosion resistance of pure Mg and AZ63 in 1000 ppm NaCl solution with pH 10 and showed that AZ63 exhibited a more positive E_{corr} and lower corrosion current density, i_{corr}, than those measured for pure Mg.

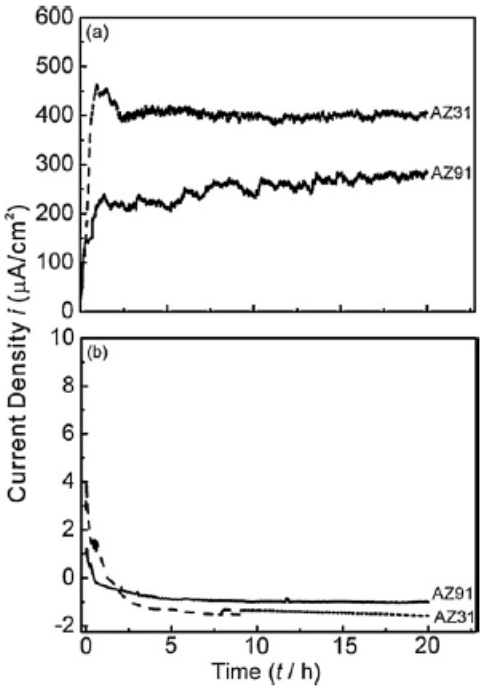

Figure 2.3 Time variation of current densities for AZ31 and AZ91 alloys polarized potentiostatically at: (a) -1.30 V and (b) -1.50 V for 20 h in 0.01 M NaCl solution [18].

Under the passivation condition, Mg alloys are protected by a relative stable surface film. Since the charge transfer of anodic reaction occurrs beneath the film, metal cations need to diffuse through the film and the film/solution interface. The mass transport rate of metal cations through either of these two layers can be rate controlling. Baril et al. [4] observed the limiting anodic current density exhibited in the polarization curves of pure Mg in 0.1 M $NaSO_4$ solution as a function of electrode rotation rate, as shown in Figure 2.4. The results indicate that the mass transport of metal cations through these two layers dominates the anodic kinetics. They also found that the rotation rate of the electrode had no effect on the polarization behaviour. Thus, the mass transport of metal cations through the surface film dominates the overall mass transport process.

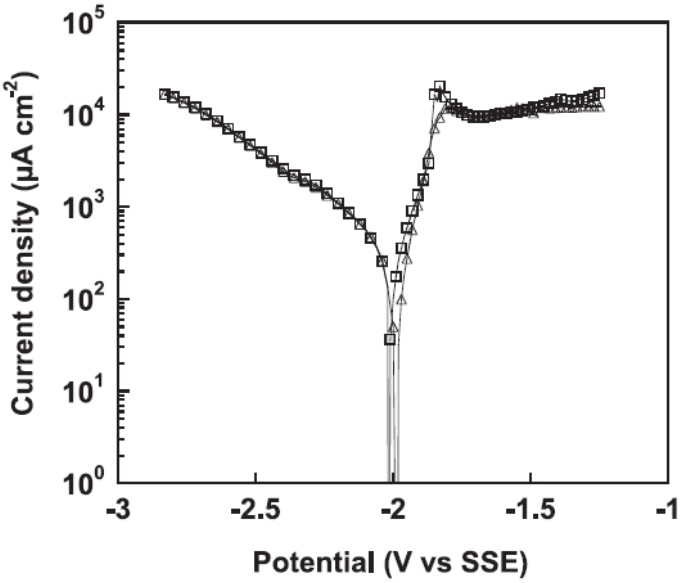

Figure 2.4 Potentiodynamic polarization curves after pre-exposure at E_{corr} in 0.1 M Na_2SO_4 solution for 3.5 h. Rotation speed: (Δ) 240 rpm; (□) 1000 rpm [4].

The corrosion resistance of Mg-Al alloys, in either state, is largely governed by the overall corrosion behaviour of pure Mg, which proceeds by an electrochemical reaction with H_2O to produce $Mg(OH)_2$ and H_2:

$$Mg + 2H_2 0 \rightarrow Mg(OH)_2 + H_2 \quad (2\text{-}1)$$

This overall reaction can be separated as shown below:

$$Mg \rightarrow Mg^{2+} + 2e^- \quad \text{(Anodic reaction)} \quad (2\text{-}2)$$

$$Mg^{2+} + 2OH^- \rightarrow Mg(OH)_2 \quad \text{(Precipitation reaction)} \quad (2\text{-}3)$$

$$2H_2O + 2e^- \rightarrow H_2 + 2OH^- \text{(Cathodic reaction)} \quad (2\text{-}4)$$

The equilibrium standard state Mg^{2+}/Mg half-cell potential (-2.37 V_{SHE}) is far more negative than the equilibrium standard state H^{+}/H_2 half cell potential (0 V_{SHE}). Consequently, the hydrogen evolution (cathode) reaction (Equation 2-4) is extensively polarized on Mg. On the other hand, the concentration of oxygen dissolved in solution is limited by diffusion. The oxygen cathodic reaction is slow compared with the hydrogen evolution reaction. Baril and Pebere [4] have shown that the steady-state cathodic current density exhibited by Mg is approximately equal in both aerated and deaerated Na_2SO_4 solution, thereby discounting any significant oxygen reduction contribution.

The Mg anodic dissolution reaction (Equation 2-2) produces the soluble Mg^{2+} ion. This ion then attracts OH^- ion in the solution to produces $Mg(OH)_2$ (Equation 2-3), which precipitates as a film on the exposed surface. The solid $Mg(OH)_2$ product is not thermodynamically stable at near-neutral pH. It is stable only after the solubility of product is exceeded, which is predicted to occur at about pH 10.5, assuming a Mg^{2+} concentration of 1×10^{-6} M [46]. For this reason, the formation of the surface film is strongly affected by pH.

The charge transfer of cathodic reaction occurs on the surface of the film [47]. The exchange current density of cathodic reaction, $i_{o,c}$, usually dominates the cathodic kinetics. It is strongly affected by the properties of the surface film. Due to the semiconducting nature of the surface film [48-49], the electron transport process is much easier and faster

than the mass transport process. Thus, the corrosion of Mg and Mg alloys are mainly controlled by the anodic process.

2.2 Localized Corrosion State ($E_{corr} > E_b$)

The majority of the corrosion research on Mg-Al alloys (both AZxx and AMxx alloys) has been developed in aggressive solutions, in which $E_{corr} > E_b$ [6, 8, 14, 21-26, 30-31, 41-42, 44, 49-58]. It is well known that they are susceptable to localized corrosion due to the breakdown of the surface film and the pit-like corrosion defects tends to propagate widely [14, 19, 22, 43, 45, 49, 56-58].

A consistent mechanism for Mg alloy film breakdown has not been established yet. Zeng et al. [43] argued that the micro-galvanic interaction between the α-matrix and an adjacent effective cathodic phase plays a major role in the passive film breakdown process, as shown in Figure 2.5. They claimed that pitting corrosion initiates at flaws in the surface film around either the β-phase or Al-Mn intermetallic phase, both of which have an electrochemical potential more positive than the α-matrix, as shown in Table 2.2. Chen et al. [59] also observed that the corrosion of AZ91 was more aggressive at Al-Mn phase regions under cyclic wet-dry conditions and the film rupture initiated at this region in the dry condition. Pardo et al. [42] observed that the pits initiated at the α matrix/Al-Mn and β-phase interface. After the Al-Mn and β-phase particles were undermined, the precipitation of the $Mg(OH)_2$ surface film on the remaining α-matrix tended to inhibit further corrosion attack. Merino et al. [31] believed that the Al-Mn particles only had a

minor influence on the early stage of passivity breakdown process. The role of these particles depended on their composition, size and location.

Table 2.2 Typical Corrosion Potential Values for Mg & Mg-Containing Second Phases (after 2 h in deaerated 5 wt % NaCl solution saturated with $Mg(OH)_2$ (pH 10.5)) [60].

Metal	**E_{corr},V_{SCE}**
Mg	-1.65
Mg_2Si	-1.65
Al_6Mn	-1.52
Al_4Mn	-1.45
Al_8Mn_5	-1.25
$Mg_{17}Al_{12}(\beta)$	-1.20
$Al_8Mn_5(Fe)$	-1.20
$Al_6Mn(Fe)$	-1.10
$Al_6(Mn\ Fe)$	-1.00
$Al_3Fe(Mn)$	-0.95
Al_3Fe	-0.74

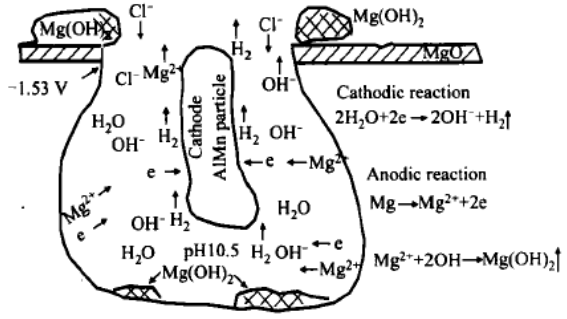

Figure 2.5 Schematic of pitting corrosion mechanism for magnesium alloy AM60 [43].

Of the three generalized aggressive ion-induced passive film breakdown models summarized by Marcus et al. [37], the most likely operating in Mg-Al alloys is the stress induced breakdown. It has been shown Cl^- can penetrate into the film to form metal-hydroxyl-chloride complex compound [8, 13, 61] . The growth of this compound can generate the stress to facilitate the breakdown of film [61] Hara et al. [5] measured the film thickness as a function of applied anodic potential using in *situ* ellipsometry. As shown in Figure 2.6, the thickness of the AZ91D film immersed in 0.1 M NaCl increased almost linearly with increasing potential from -1.5 $V_{Ag/AgCl}$ to -1.36 $V_{Ag/AgCl}$. The film thickness reached a constant value once the potential exceeded E_b. This suggests that the film growth is interrupted when the alloy undergoes passivity breakdown.

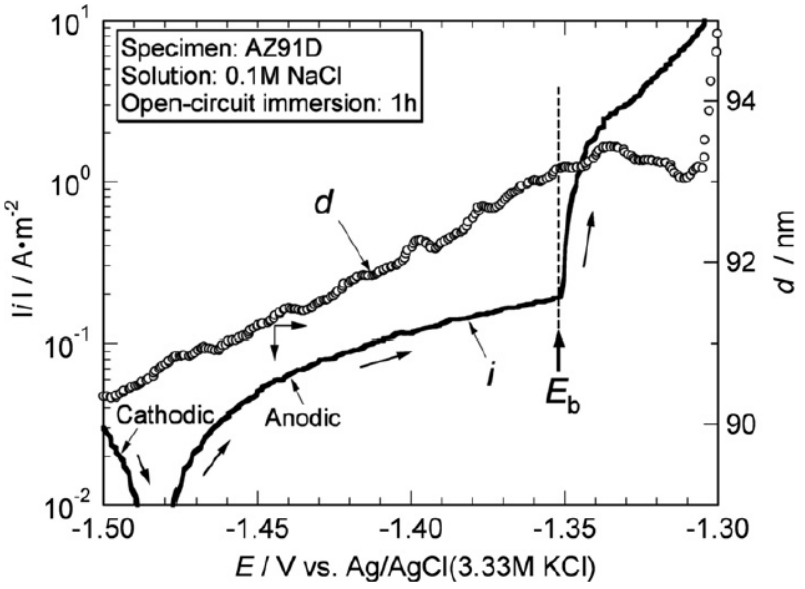

Figure 2.6 Changes in current density and thickness of surface films as a function of potential during anodic polarization of AZ91D in 0.1 M NaCl. Polarization started after immersion for 1 h [5].

Brun et al. [8] utilized infrared spectroscopy and XRD to identify the presence of chloride containing compounds corresponding to $MgCl_2 \cdot 6H_2O$ and $Mg_3(OH)_5Cl \cdot 4H_2O$ located in the surface film formed on Mg, which was immersed in 3 wt % NaCl solution at E_{corr}. This is consistent with the observation by Lindström et al. [7] on the surface film formed on NaCl-coated (70 μg/cm^2) AZ91 after exposure to a humid environment (95% relative humidity). The formation of the soluble metal-hydroxyl-chloride complex compound results in the favourable anodic dissolution of Mg accompanied by the chemical dissolution of the surface film. In addition, Yao et al. [62] observed that the corrosion product formed on pure Mg in 3 wt % NaCl solution was more hydrated, and became more porous and thicker than the films formed in distilled water (Table 2.3). Wang et al. [18] , however, did not find any evidence of Cl^- ion incorporation within the surface film formed on AZ31 and AZ91 in dilute NaCl solution (0.01 M) at an anodic potential both above and below E_b. The surface film observed was mainly a mixture of $Mg(OH)_2$ and $MgCO_3$. They claimed that the CO_2/HCO_3^- could compete with Cl^- to affect the surface film formation and breakdown depending on the concentration of anions. The degree of carbonation was found to be lower in the corrosion zone than in the passivation zone. Dissolved CO_2 from atmosphere and the presence of HCO_3^- showed inhibited effect due to the formation of $MgCO_3$, which could enhanced the passivity of surface layer and minimized chloride-induced corrosion on the alloy [24]. This is consistent with the observations by Lindström et al. [7] on the surface film formed on NaCl-coated (70 μg/cm^2) AZ91 after exposure to a humid environment (95% relative humidity) in the presence of CO_2. Merino et al. [31] studied the influence of Cl^- concentration and

temperature on the corrosion of AZ31B alloy using salt fog. The corrosion products formed on AZ31 at higher temperatures (35°C) were less rigid and less protective than the corrosion product formed at lower temperatures (25°C). Thus, environmental factors, such as the concentration of anion and the temperature, have a significant influence on the chemical composition and structure of the surface film, and consequently affect the corrosion resistance of Mg alloys and the film breakdown process.

Table 2.3 Oxide Film Thickness (nm) Estimated by XPS for Melt-Spun Mg Ribbon in Three Conditions for Various Duration [62].

Condition	**1 min**	**3 h**	**7 days**	**1 month**	**7 years**
Air	2.65	N/A	5.31	5.54	5.67
Distilled water	11.20	28.71	N/A	N/A	N/A
3 wt % NaCl	15.43	30.44	N/A	N/A	N/A

Increasing Al concentration has been found to decrease the corrosion rate of Mg-Al alloys in saline solutions [24-25, 42, 56, 58]. Song et al. [25] studied the electrochemical polarization behaviour of solution-treated Mg-Al single α-phase alloys with various Al concentrations after immersion in 5 wt % NaCl solution (pH 11) for 3 h. They observed that all alloys exhibited an E_{corr} above E_b. In addition, both E_b and E_{corr} increased with an increase in the α-phase Al content (Figure 2.7). It is interesting to see the significant reduced cathode kinetics as the Al content increases. Furthermore, their similar potentiodynamic polarization tests done for pure Mg, α-phase (AZ21), β-phase (AZ501) and dual phase alloy (AZ91) in 1 M NaCl solution shows that the cathodic kinetics are

affected not only by Al content in α-Mg matrix, but also by the presence of β-phase (Figure 2.7) [24].

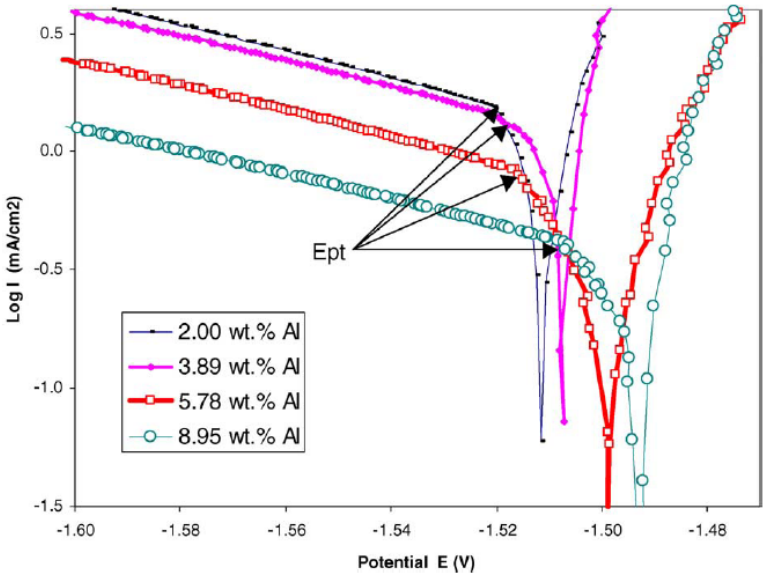

Figure 2.7 Polarization curves of Mg-Al single α-phase alloys in 5 wt % NaCl saturated with $Mg(OH)_2$ (pH 11) [25].

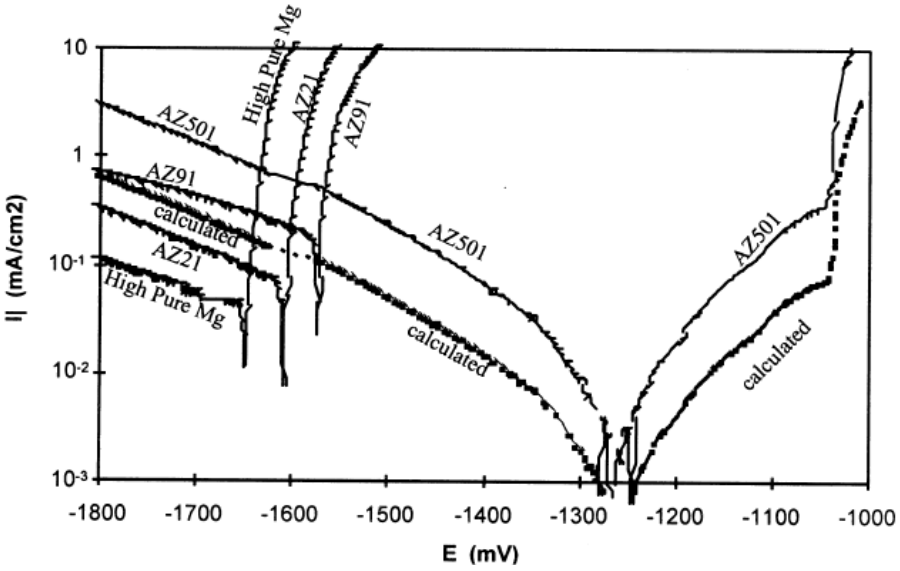

Figure 2.8 Polarization curves for pure Mg, AZ21 (α), AZ501 (β) and AZ91 (α+β) in 1 M NaCl (pH 11) [24].

As inferred from Table 2.2, the β-phase is cathodic to the α-phase. Song et al. [24] measured the polarization behaviour of both the α-phase and β-phase in 1 M NaCl at pH 11, as shown in Figure 2.8. They found that the β-phase has more positive E_{corr} and exhibits lower i_{corr} than the α-phase. This agrees very well with the work done by Lunder et al. [44]. They observed that β-phase exhibited more positive E_{corr} and lower corrosion rate than those measured on pure Mg in 5 wt % NaCl solution. Song et al. [56-58] proposed that the β-phase has two influences on corrosion resistance of Mg-Al alloys depending on its volume fraction and distribution in the matrix. This phase could act as a barrier to inhibit corrosion or as an efficient galvanic cathode to accelerate the corrosion process of the α-Mg matrix. This proposed dual role of β-phase is supported by the study on the heat-treatment effect on corrosion resistance of AZ91D [25, 27, 44, 53]. An increase in aging time of the T4 condition was found to cause discontinuous β-phase precipitation along grain boundaries and a reduction in the Al content in the α-matrix. This caused the enhanced micro-galvanic corrosion to accelerate the anodic dissolution of α matrix [25], as shown in Figure 2.9. However, Lunder et al. [44] disagreed with this. They claimed that the cathodic activity of β-phase is very small when it coupled with α-phase. They attributed the preferential corrosion attack of the α-phase to a higher intrinsic dissolution rate.

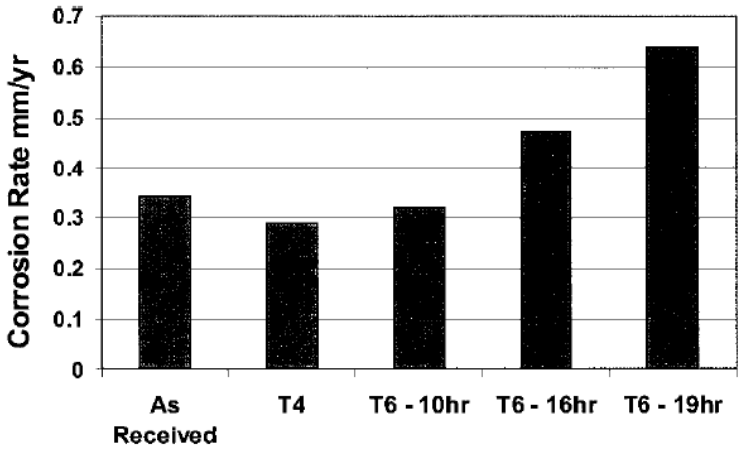

Figure 2.9 Weight loss represented as corrosion rate for heat treated AZ91 samples immersed for 100 h in 0.1 M NaCl [44].

The proposed dual role of β-phase also has been used to explain the improved corrosion resistance of die-cast skin of Mg alloys. The skin of die-cast AZ91D showed significantly more corrosion resistance (one order of magnitude lower corrosion rate) than its interior when tested in at E_{corr} in 1 M NaCl pH 11 [21]. This could be attributed to more continuous β-phase around finer grain boundaries in the skin (Figure 2.10), where the β-phase acted as a barrier to corrosion propagation. Song et al. [21] schematically illustrated the skin effect as shown in Figure 2.11. If the grains are very fine and the fraction of β-phase is not too low, the β-phase can build a nearly continuous network around the α-matrix and inhibit corrosion attack. In addition, the corrosion products formed will easily deposit on the surface due to the slower corrosion reaction. This will be beneficial in order to further slow down the corrosion process.

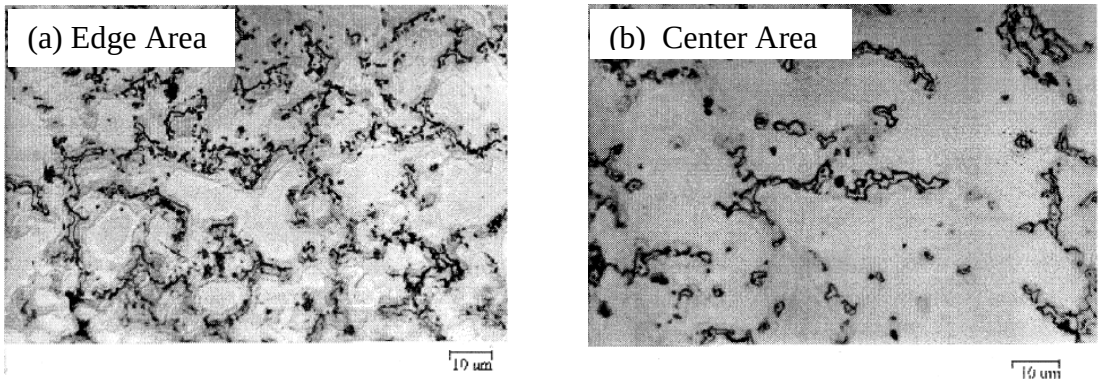

Figure 2.10 Optical microstructures after etching of different sections of die-cast AZ91D alloy: (a) edge area, (b) center area [21].

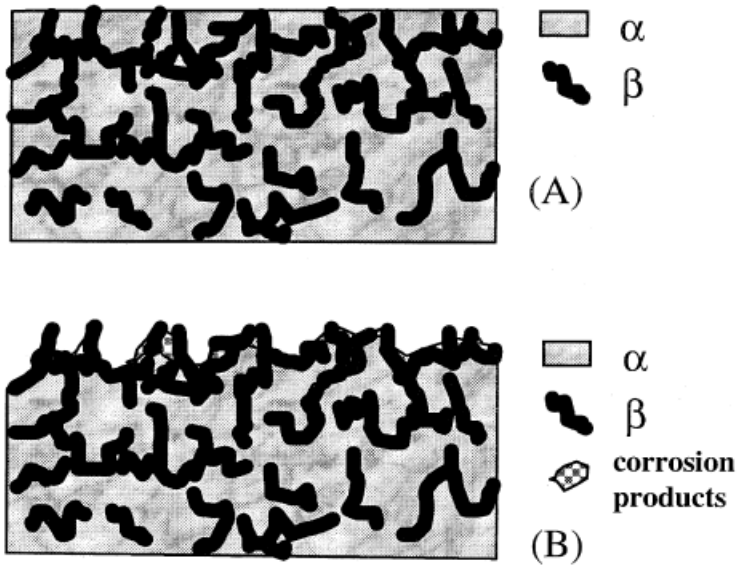

Figure 2.11 Schematic presentation of the change of surface composition during corrosion for an alloy with nearly continuous β-phase over its surface layer: (A) initial surface, (B) final surface [21].

The addition of Zn to AZxx alloys is limited to 1 to 3 wt % due to its accelerating effect on corrosion above 3 wt % [60]. Zn may be present in both the α-matrix and the β-phase. Daloz et al. [50] reported that the addition of Zn increased E_{corr} and decreased i_{corr} of both the α-Mg matrix and β-phase in ASTM D 1384 solution (Table 2.4). This effect is

consistent with the corrosion performance of Zn within the α and β phase after electrochemical testing in 5 wt % NaCl solution saturated with $Mg(OH)_2$ [44]. Song et al. [57] showed that during the anodic dissolution of AZxx, Mg was the main component dissolving into solution and there was no dissolved Zn was found in the solution. Song [24] analyzed the surface film formed on AZ21, AZ501 and AZ91 after 24 h exposure in 1 N NaCl at pH 11 using XPS. The surface film on all alloys did not contain any Zn. In addition, a small amount of Zn was found to have dissolved into the test solution for all Mg alloys tested. This suggests that Zn was not involved in the surface film formation process.

Table 2.4 Electrochemical Behaviour of Various Phases in ASTM D1384 Solution (0.148 g/L Na_2SO_4 + 0.138 g/L Na_2CO_3 + 0.165 g/L NaCl) [50].

Alloy	**E_{corr}, 2 h (v)**	**R_p, 2 h (kΩ)**	**E_{corr}, 4 h (V)**	**R_p, 4 h (kΩ)**	**i_{corr}, 4 h ($\mu A/cm^2$)**
Mg-4% Al	-1.84	1.05	-1.82	1.15	215
Mg-7% Al	-1.79	1.14	-1.76	-1.25	162
Mg-6.5% Al-0.5%Zn	-1.41	4.7	-1.31	20.9	12
$Mg_{17}Al_{12}$	-1.51	4.75	-1.46	5.61	32
$Mg_{17}Al_{15}$	-1.56	4.80	-1.50	6.02	11
$Mg_{17}Al_{18}$	-1.45	14.5	-1.41	20.5	4.5
$Mg_{17}Al_{11}Zn_1$	-1.32	4.7	-1.23	11	68
$Mg_{17}Al_{10}Zn_2$	-1.28	2.2	-1.21	16.3	7.4

2.3 Passive Corrosion State ($E_{corr} < E_b$)

Comparing to the extensive corrosion research on the localized corrosion state (above E_b), there is significantly less reported about the influence of the controlling factors on the corrosion resistance of Mg-Al alloys exhibited below E_b.

Nordlien et al. [15-16] reported a three-layer surface film structure (Figure 2.12) when Mg-Al alloys exposed in distilled water for 48 h. A dense intermediate layer was the initial air-formed film, which consisted of amorphous MgO enriched with Al. The outer platelet-like layer mainly consisted of crystalline $Mg(OH)_2$, which was formed by dissolution-precipitation reaction (Equation (2.3)). They believed that the Al-rich inner layer plays a major role to improve the corrosion resistance of Mg-Al alloys. Wang et al. [18, 20] used XPS to study the chemical composition of the surface film formed on AZ31 and AZ91 alloys after exposure to 0.01 M NaCl solution in the passivation zone. The outer layer consisted of $Mg(OH)_2$ and $MgCO_3$, while the inner layer was a mixture of $Mg(OH)_2$, MgO and $MgCO_3$. They claimed that the formation of $MgCO_3$ retards the Cl^- induced corrosion, and consequently the carbonation degree affects the properties of corrosion or passivation zone of Mg-Al alloys. The *ex situ* and *in situ* film study by Santamaria et al [17] found that the structure of the initial film formed on Mg in aqueous solutions consisted of a non-compact duplex structure containing a thick and porous external layer of $Mg(OH)_2$. Furthermore, a non-ordered region can form between crystalline grains during the growth process, creating a grain boundary [61]. The passive film formed on non-ordered region provides partial protection to the substrate metal.

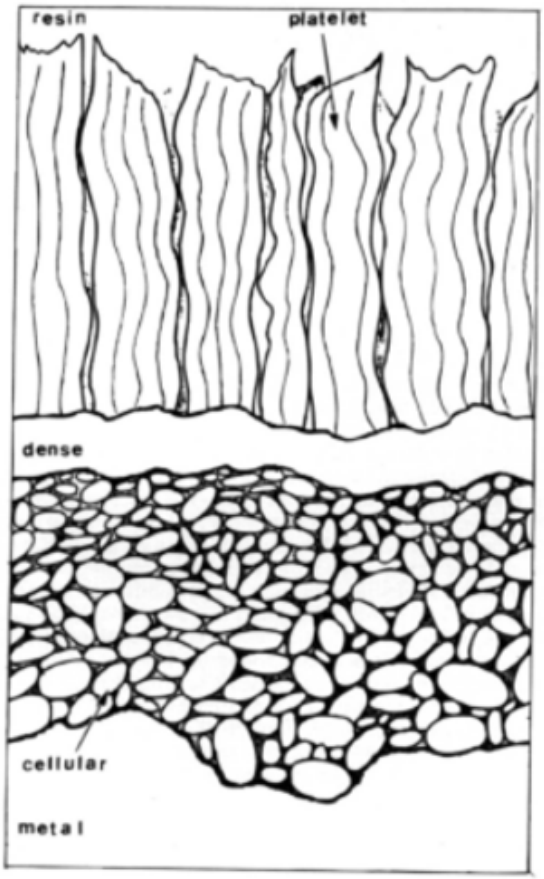

Figure 2.12 Schematic representation of the surface film formed on Mg and its alloys after 48 h exposure to distilled water [15-16].

Nordlien et al. [15] analyzed the Al distribution in the surface film formed on Mg-Al alloys, as shown in Figure 2.13 and Figure 2.14. They found that Al was mostly distributed in the inner layer. An increase in Al content above 3~5 wt % in alloy dramatically decreases the thickness of the outer platelet layer, as shown in Figure 2.15. This resulted in a thinner and compact surface film and consequently improved the corrosion resistance of Mg-Al alloys. Splinter and McIntyre [63] claimed that the bulk thickening process in D_2O water vapour environment was controlled by the transport of

metal cations through the film. The Al addition resulted increase activation energies and, thus decreased the rate of oxide film growth.

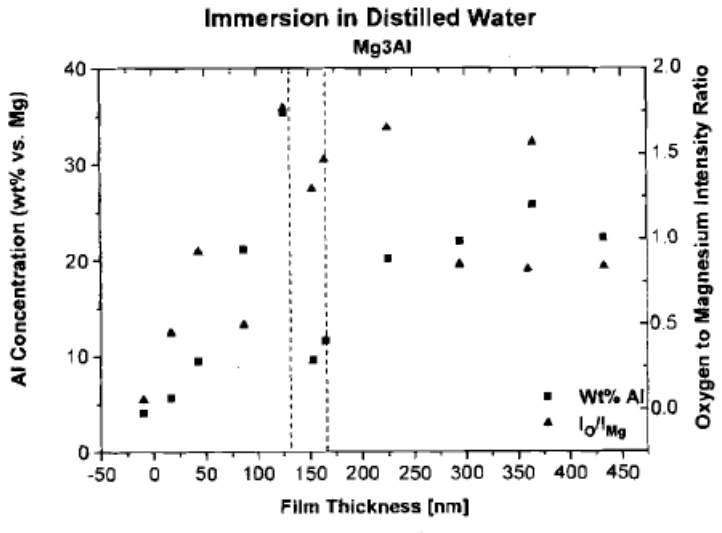

Figure 2.13 Al concentration and O/Mg ratio depth profiles of oxide film on Mg-3 % Al specimen using X-ray EDS point analysis after immersion in distilled water for 48 h [15].

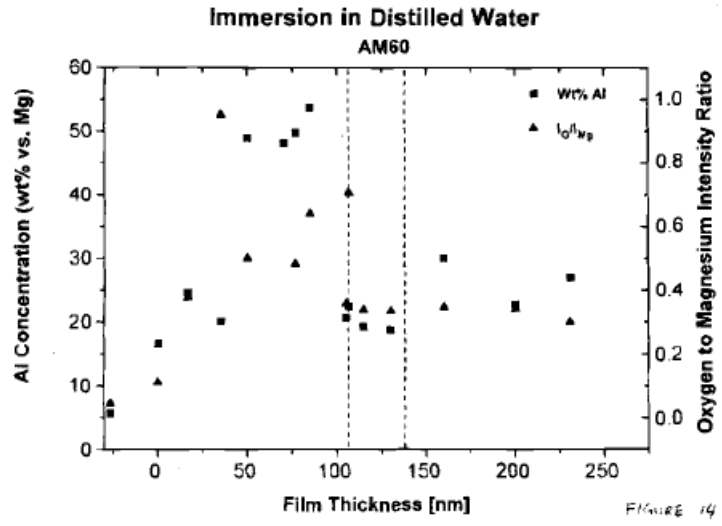

Figure 2.14 Al concentration and O/Mg ratio depth profiles of oxide film on AM60 specimen using X-ray EDS point analysis after immersion in distilled water for 48 h [15].

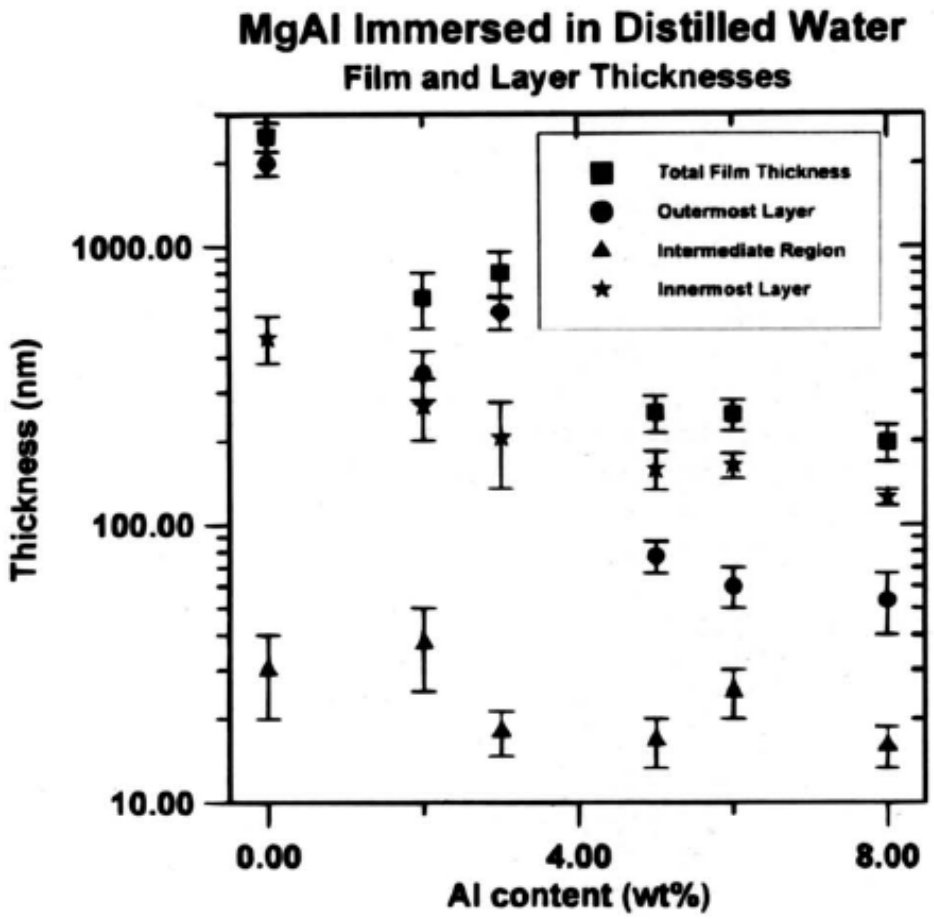

Figure 2.15 Total film thickness and layer thickness of the oxide film as a function of Al content of the alloy [15].

Hara et al. [5] found the film formed on AZ91D grew rapidly in two consecutive stages; stage one where the film thickness increased linearly with time, and stage two where the film growth rate decreased with time (Figure 2.16). They also observed the increased E_b and reduced passive current density, i_{pass}, with film growth when AZ91D exposed in 0.1 M NaCl solution for longer time. Comparing with pure Mg, the increasing rate of E_b and

decreasing rate of i_{pass} with film thickness for AZ91D is larger, which could be attributed to the change in composition and structure of surface film. They believed that the increased resistance of thicker film might slow down the electrochemical reaction that occurred on the exposed surface and consequently reduce the corrosion rate. Thus, the film growth of Mg alloy might suggest two aspects for corrosion research. First, pre-exposing Mg alloy in dilute solution improves its corrosion resistance [5]. Second, the long term corrosion test result might not agree with the short electrochemical test results, which indeed has been reported [54].

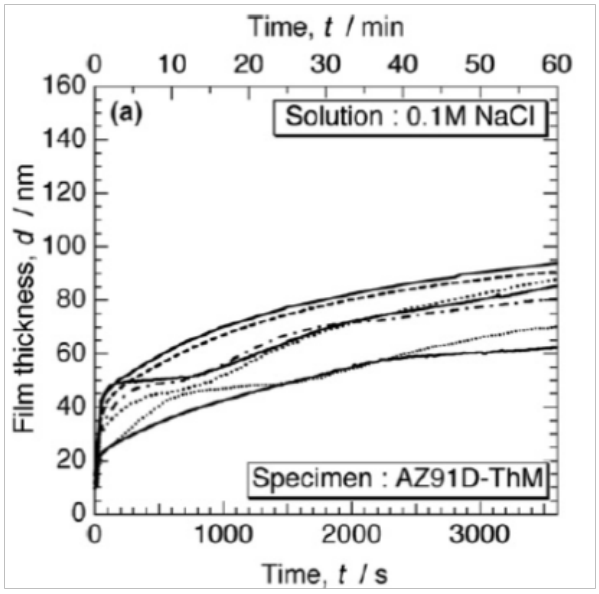

Figure 2.16 Thickness of surface film formed on AZ91D as a function of immersion time in 0.1 M NaCl [5].

2.4 Relative Corrosion Behaviour

Mg-Al alloys exhibit very good atmospheric corrosion resistance [3, 9, 11, 13, 60, 64]. Table 2.5 summarizes the reported corrosion rate of Mg and Mg alloy in different atmospheric environments. It is clear that higher Al content alloys exhibit better corrosion resistance. The overall ranking of Mg-Al alloys corrosion rate in the passive state is given as Mg > AZ31 > AZ80 > AZ91D. Lindström et al. [7] observed the localized corrosion occurred on AZ91D in the absence of CO_2, in contrast, pitting is inhibited in the presence of CO_2 with relatively uniform corrosion product development. The inhibitive effect of CO_2 was also observed in the long-term exposures, showing that CO_2 reduces the average corrosion rate.

Most of the research reporting has utilized aggressive solutions such as 3~5 wt % NaCl [5, 23-24, 26, 41-42, 44, 62], in which E_{corr} is above E_b, to compare the corrosion resistance of Mg alloys. Cheng et al. [41] compared the corrosion resistance of Mg alloy in 1 M NaCl solution using EIS and potentiodynamic polarizaion. They reported the relative corrosion rate is ranked as AZ91>AZ31>AM60. By contrast, Zhao et al. [29] did same potentiodynamic test in 3 wt % NaCl solution and gave the rank of corrosion rate as AZ31>AM30>AM60≈AZ91. This relative ranking also disagreed with their long term salt spray and hydrogen evolution test results, as shown in Table 2.6. These conflicting results indicate that these normal corrosion tests on Mg alloys in aggressive solution are not reliable. In aggressive solution, Mg alloys undergo severe localized corrosion. In this case, the anodic current density increases dramatically with an increase in the polarization

potential. These relative deviations were much larger than the precision of the electrochemical method. Song and Atrens [58] found Tafel extrapolation could not estimate the corrosion rate reliably. Shi et al. [54] reported that the relative deviation in the evaluation of the corrosion rate from Tafel extrapolation ranged from 48% to 96% when Mg alloys test in 3.5 wt % NaCl solution. Thus, comparing Mg alloys corrosion rate in aggressive solution is not suitable for the application in automotive industry.

Table 2.5 Atmospheric Corrosion Rate of Mg and Mg alloys.

Alloy	**Test Condition**	**Corrosion Rate (mg/cm^2)**			**Ref.**
		7 days	**15 days**	**30 days**	
AZ91	95% RH, 22°C	-	-	~0	[13]
Mg	95% RH, 22°C	-	-	0.01	[7]
Mg	98% RH, 50°C	0.06	0.12	0.17	[11]
AZ31	98% RH, 50°C	0.03	0.08	0.12	[11]
AZ80	98% RH, 50°C	0.008	0.034	0.057	[11]
AZ91D	98% RH, 50°C	0.014	0.053	0.072	[11]
AZ91D	95% RH, 22°C,15 μg/cm^2 NaCl added	-	-	0.1	[13]
AZ91D	95% RH, 22°C,36 μg/cm^2 NaCl added	-	-	0.17	[13]
AZ91D	95% RH, 22°C,74 μg/cm^2 NaCl added	-	-	0.23	[13]
AZ91D	95% RH, 25°C,70 μg/cm^2 NaCl added	0.15	0.3	0.47	[3]
AM20	95% RH, 22°C,70 μg/cm^2 NaCl added	0.33	0.6	0.73	[64]
AM60	95% RH, 22°C,70 μg/cm^2 NaCl added	0.26	0.36	0.5	[64]
AZ91D	95% RH, 22°C,70 μg/cm^2 NaCl added	0.18	0.21	0.23	[64]
AZ31	Continuous condensation, 100% humidity, 23°C	0.07	0.15	0.38	[9]
AZ61	Continuous condensation, 100% humidity, 23°C	0.23	0.21	0.36	[9]

Table 2.6 Comparison of Corrosion Rate of Mg Alloys.

Alloy	**Test Condition**	**Corrosion Rate**	**Ref.**
AZ31	Salt spray, 3% NaCl ,7 days	0.3 mm/yr	[29]
AM30	Salt spray, 3% NaCl ,7 days	0.3 mm/yr	[29]
AM60	Salt spray, 3% NaCl ,7 days	2.3 mm/yr	[29]
AZ91	Salt spray, 3% NaCl ,7 days	0.9 mm/yr	[29]
AZ31	Hydrogen evolution, 3% NaCl, 7 days	2.3 mm/yr	[29]
AM30	Hydrogen evolution, 3% NaCl, 7 days	8.7 mm/yr	[29]
AM60	Hydrogen evolution, 3% NaCl, 7 days	9.3 mm/yr	[29]
AZ91	Hydrogen evolution, 3% NaCl, 7 days	4 mm/yr	[29]
AZ31	Potentiodynamic polarization, 3% NaCl	0.7 mm/yr	[29]
AM30	Potentiodynamic polarization, 3% NaCl	0.5 mm/yr	[29]
AM60	Potentiodynamic polarization, 3% NaCl	0.2 mm/yr	[29]
AZ91	Potentiodynamic polarization, 3% NaCl	0.2 mm/yr	[29]
AZ31	Potentiodynamic polarization, 3% NaCl	5.3 mm/yr	[41]
AM60	Potentiodynamic polarization, 3% NaCl	3.4 mm/yr	[41]
AZ91	Potentiodynamic polarization, 3% NaCl	10.84 mm/yr	[41]

2.5 Knowledge Gaps

Throughout the literature review, it is clear that the factors controlling the corrosion resistance of Mg-Al alloy are significant different for the corrosion states: localized corrosion and passivation. Standard salt fog testing (e.g. ASTM B117) and immersion testing in 3~5 wt % NaCl solution are commonly used for corrosion studies, in which Mg alloys suffer severe localized corrosion and exhibit extremely high corrosion rates [3, 8, 13, 21-31, 65]. However, the typical automotive road environment is mildly aggressive [60, 66], in which Mg alloys are likely exposed in the passive state. It is important to understand the corrosion resistance of Mg alloy before and after the protective surface breakdown. In addition, it is necessary to identify which metallurgical and environmental factors critically affect the corrosion resistance of Mg alloys in passive state and what are the controlling factors affecting the surface film breakdown. Obviously, a mildly aggressive corrosion environment is more suitable for Mg alloy corrosion research to indentify the subtle yet important difference in corrosion behaviour for automotive use. Electrochemical testing in solution is great to help understand the corrosion resistances of Mg alloys when combined with salt fog testing.

Chapter 3. Objective

This research is intended to systematically investigate the corrosion resistance of the MFERD alloys (rolled AZ31B, extruded AM30 and die-cast AM60B) in near-neutral saline environments. The research objectives devised to achieve a better understanding of the influence of metallurgical factors and environment variables on the corrosion resistance of Mg-Al alloys in both the localized corrosion and partially passive state including the following:

1. Compare electrochemical behaviour of AZ31B, AM30 and AM60B, in mildly aggressive near-neutral saline solution to indentify the subtle yet important differences in cathodic & anodic processes.
2. Investigate the critical factors controlling the corrosion resistance and surface film breakdown process of Mg-Al alloys.
    - Influence of metallurgical factors: alloying elements (Al, Zn), crystallographic extrusion texture, presence of β-phase ($M_{g17}A_{12}$) and Al-Mn intermetallic particles.
    - Influence of environment: pre-exposure time and applied potential.

Chapter 4. Experimental Procedures

4.1 Materials Characterization

4.1.1 Materials

Three MFERD magnesium alloys were used in this research: high pressure die-cast AM60B sheet with a thickness of 1.6 mm, extruded AM30 bar with a 15 x 25 mm^2 cross-sectional area and rolled AZ31B sheet with a thickness of 1.44 mm. Figure 4.1 shows the rolled AZ31B plate, extruded AM30 bar and cast AM60B plate.

The chemical composition of these alloys was determined by Inductively Coupled Plasma (ICP) spectrometry and the results are shown in Table 4.1. AZ31B and AM30 both contained similar concentrations of Al. However, AZ31B contains approximately 1 wt % Zn, which was only present in trace amounts in AM30. The main composition difference between AM30 and AM60B is that AM60B contains approximately twice as much Al. The concentration of Mn in all three alloys was similar. All other elements, such as iron and silicon, were below the respective maximum tolerance level.

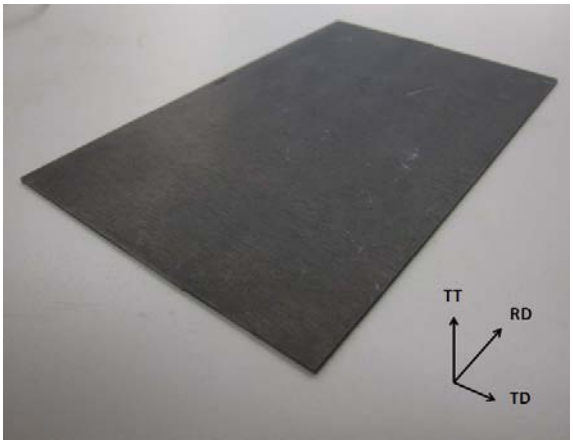

(a) As-rolled AZ31B

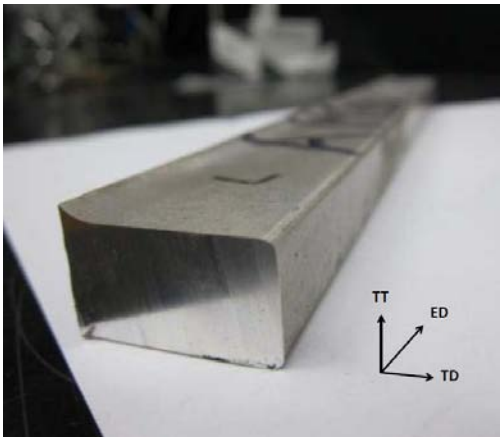

(b) As-extruded AM30

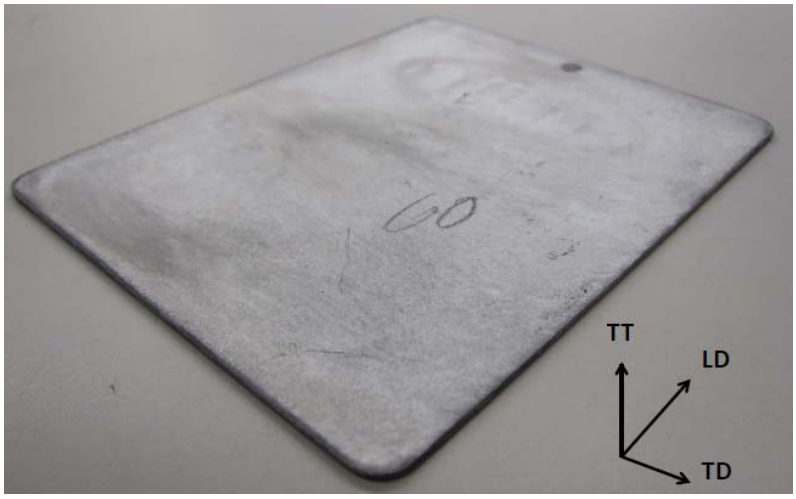

(c) As-cast AM60B

Figure 4.1 Images of as-received MFERD magnesium alloys.

Table 4.1 Chemical Composition of Experimental Alloys (wt %).

Alloy	**Condition**	**Al**	**Zn**	**Mn**	**Fe**	**Si**	**Mg**
AZ31B	As-rolled	3.146	0.955	0.433	0.002	0.015	Balance
AM30	As-extruded	2.681	0.002	0.420	0.014	0.003	Balance
AM60B	As-cast	5.603	0.098	0.340	0.007	0.022	Balance

4.1.2 Metallography

Optical Microscopy was used to observe the microstructures prior to corrosion testing and the extent of corrosion damage in the cross-section after exposure. The bulk material was cut into small pieces using the chop saw with water cooling. Then all specimens were sectioned using a precision cutting machine at a vertical cutting speed of 0.005 mm/s with water cooling. All samples were cold mounted in epoxy resin. The grinding and polishing procedures employed for all samples are shown in Table 4.2.

AZ31B and AM30 specimens were etched in 6 g (picric acid), 5 ml (acetic acid), 10 ml (water) and 80 ml (ethanol 95%) to define the grain boundaries, while AM60B samples were etched in 10 ml (HF 48%), 90 ml (water) to darken the β-phase ($Mg_{17}Al_{12}$) [35].

Table 4.2 Polishing Procedure for Magnesium Alloys.

Step	Surface	Abrasive	Lubricant	Load (N)	Time (min)
1	Paper	SiC 1200 grit	Water	10	1.5
2	Paper	SiC 2400 grit	Water	10	0.5
3	Paper	SiC 4000 grit	Water	10	0.5
4	MD-Nap Cloth	Water-free 9 μm diamond suspension	20% (ethylene glycol) +80% (ethanol 100%)	10	5
5	MD-Nap Cloth	Water-free 3 μm diamond suspension	20% (ethylene glycol) +80% (ethanol 100%)	10	5
6	MD-Chem Cloth	Metlab-OPS (Water based 0.05 μm colloidal silica)	N/A	10	10

Rolling Direction (RD), Transverse Direction (TD) and Through Thickness (TT) directions were used to define the three planes of the AZ31B sheet as shown in Figure 4.1(a). The rolling surface was the RD-TD plane and the other cross-sections were defined as the RD-TT and TD-TT planes, respectively. Figure 4.2 presents the single phase microstructure of the as-received AZ31B. The grains were slightly elongated along the rolling direction. Extensive twinning was observed in all three planes, and this made it very difficult to evaluate corrosion damage in this state. Thus, it was necessary to recrystallize the AZ31B. Heat treatments were carried out on AZ31B samples under the following conditions: 350°C for 3 h, 350°C for 6 h and 400°C for 24 h. The samples were furnace cooled. The microstructure of the AZ31B sample after annealing at 350°C for 6 h is presented in Figure 4.3. A single phase microstructure without twins was observed.

Equaxied grains were homogeneously distributed for all planes. A small amount of Al-Mn intermetallics were randomly distributed in the α-Mg matrix. The microstructures were similar for the heat treatment conditions of 350°C for 3 h and 400°C for 24 h. The average grain sizes for the various heat treatments are shown in Table 4.3. At 350°C, the average grain size was similar after heat treatment for 3 and 6 hours. However, at 400°C the grain size was much larger. Therefore, to ensure complete recrystallization and limited grain growth, a heat treatment of 350°C for 6 h was applied on all AZ31B samples prior to further testing.

Table 4.3 Average Grain Size after Different Heat Treatment for AZ31B.

Heat Treatment	Average Grain Size (μm)
350°C for 3 h	9
350°C for 6 h	10
400°C for 24 h	17

As shown in Figure 4.1(b), Extrusion Direction (ED), Transverse Direction (TD) and Through Thickness (TT) direction were used to define the three planes of the extruded AM30. The two extrusion surfaces were the ED-TD and ED-TT planes; the cross-section perpendicular to the extrusion direction was the TD-TT plane. Figure 4.4 presents polarized light optical composite microstructures of the ED-TT and TD-TT planes from the skin to center. The microstructure of the TT-TD plane could be observed by bright field and polarized light, while the ED-TT plane microstructure could only be observed by polarized light. This suggests that the preferred crystallographic texture on these two

planes was different. For this reason, polarized light was used on all planes for the analysis of the AM30 microstructure. The as-extruded AM30 had a skin layer with a thickness of approximately 200 μm containing coarse grains, as shown in Figure 4.4. The average grain size gradually decreased from the skin to the central region of the sample. In addition, the grains were slightly elongated along the extrusion direction. Figure 4.5 shows the microstructure of AM30 at higher magnification in the central region for the three planes. The microstructure was essentially a single phase, which contained some Al-Mn intermetallics randomly distributed in the α-Mg matrix. Some small grains mixed with larger grains comprised the bimodal grain size distribution observed.

As shown in Figure 4.1(c), Longitudinal Direction (LD), Transverse Direction (TD) and Through Thickness (TT) direction were used to define the three planes of the cast AM60B. Figure 4.6 shows the optical metallographic images of as-cast AM60B at the skin region and at the central region. AM60B showed a dual phase microstructure. The dark β-phase precipitated along grain boundaries and built a semi-continuous network around the α-Mg phase. In the skin region there were higher volume fractions of β-phase and the grain size was smaller than that of the central region. Furthermore, a more dispersed area fraction of this β-phase network was observed in the central region. Also, there were some voids in the central region that were larger than the grain size, which was approximately 1 μm. By contrast, fewer voids were observed in the as-cast skin region.

Unlike AZ31B, extensive twinning was not observed in either AM30 or AM60B. For this reason, corrosion attack could be easily evaluated in the as-received condition and, therefore, it was not necessary to do heat treatments on AM30 and AM60B.

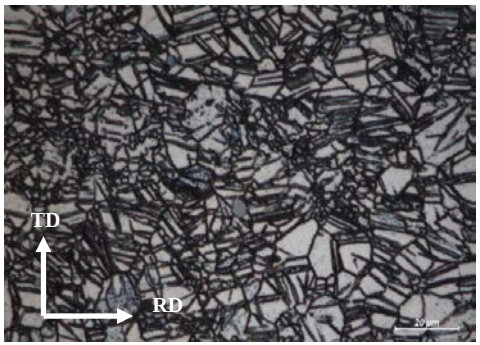

(a) As-received AZ31B RD-TD plane

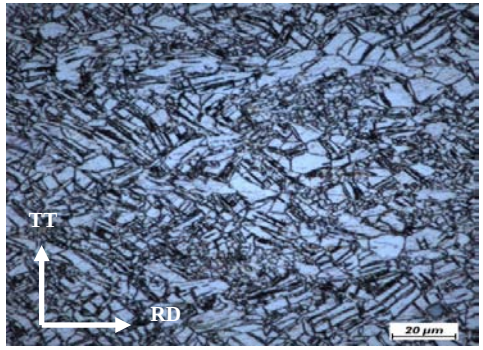

(b) As-received AZ31B RD-TT plane

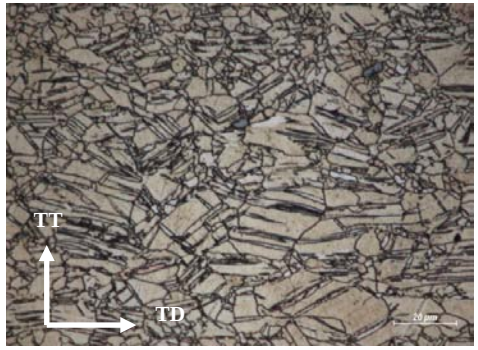

(c) As-received AZ31B TD-TT plane

Figure 4.2 Optical microstructure of as-received AZ31B.

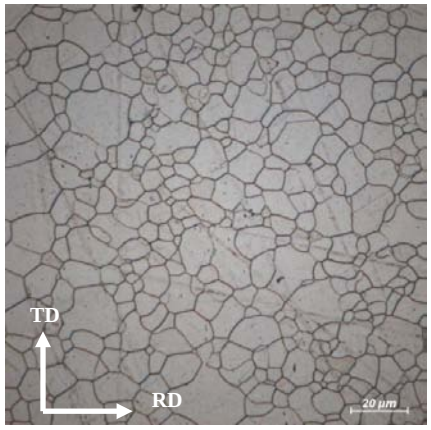

(a) AZ31B RD-TD plane

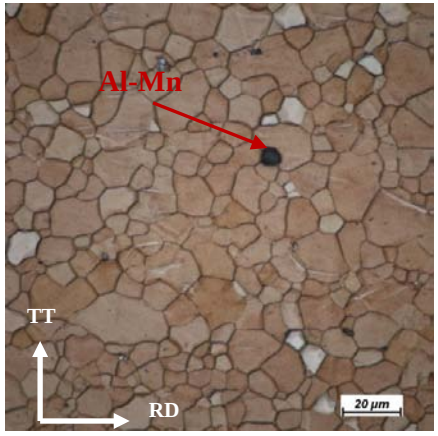

(b) AZ31B RD-TT plane

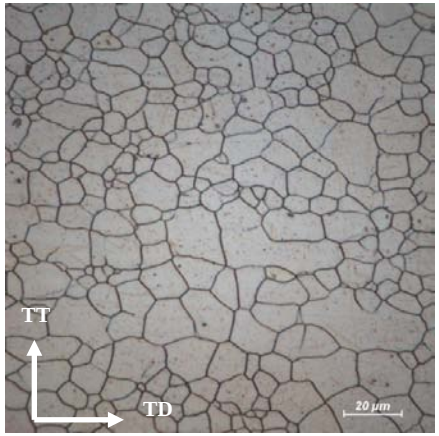

(c) AZ31B TD-TT plane

Figure 4.3 Optical microstructure of AZ31B after heat treated at 350°C for 6 h and furnace cooled.

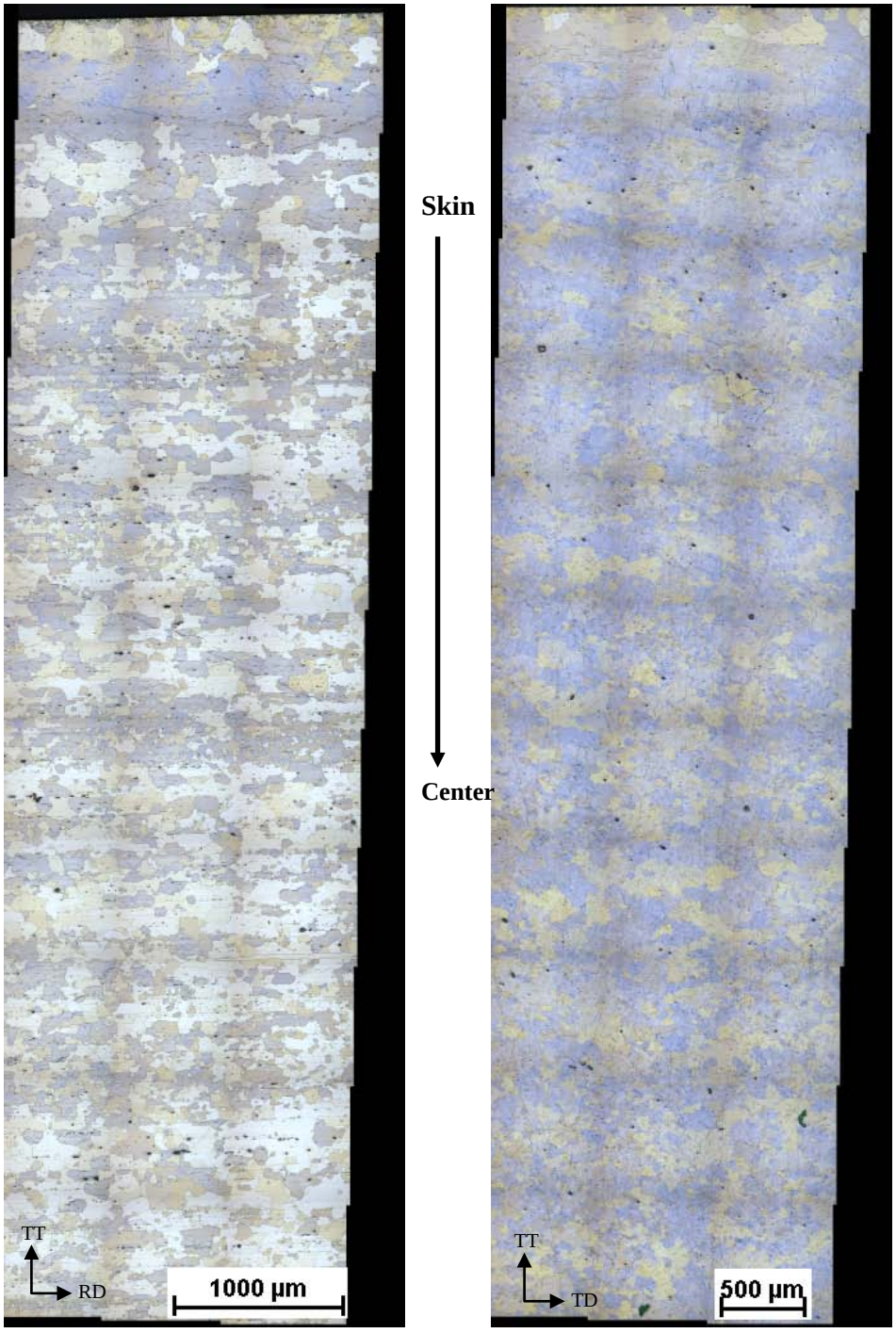

(a) ED-TT plane (b) TD-TT plane

Figure 4.4 Through thickness microstructure of as-extruded AM30 for the ED-TT and TD-TT planes.

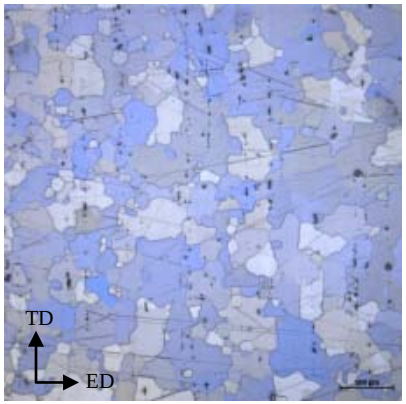

(a) ED-TD plane

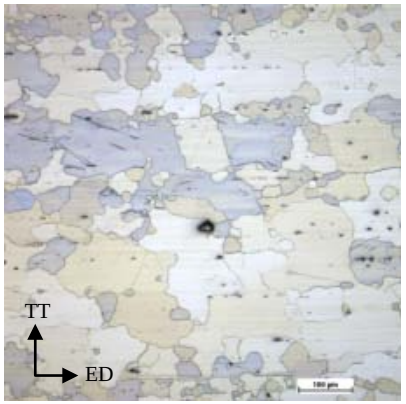

(b) ED-TT plane

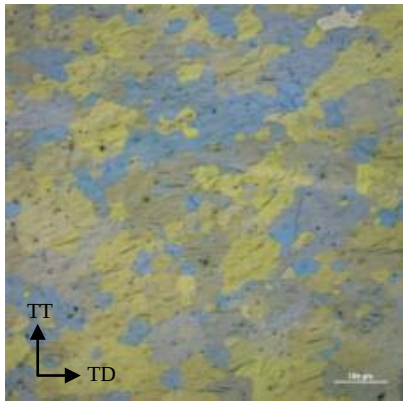

(c) TD-TT plane

Figure 4.5 Polarized optical microstructure of as-extruded AM30.

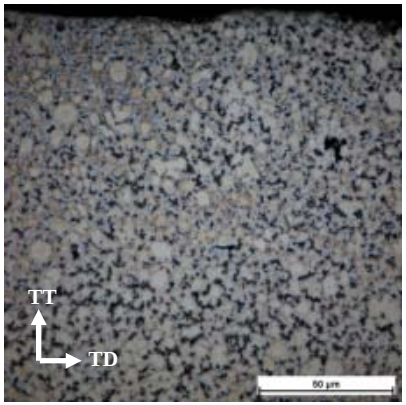

(a) Skin region

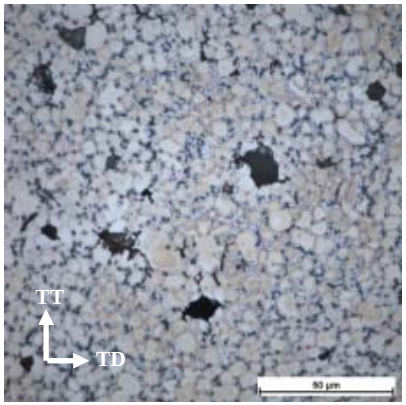

(b) Center region

Figure 4.6 Optical microstructure of as-cast AM60.

4.1.3 Microhardness Tests

Microhardness tests were performed utilizing a CLEMEX CMT 5.0 microhardness testing system. A Vickers indenter was used with a 100 g load and a dwell time of 10 s to obtain hardness profiles along the cross-section of each alloy. Samples were cold mounted and polished up to 0.05 μm Al_2O_3 to ensure a flat surface. Tests were completed on ED-TT and TT-TD planes along three lines in a grid pattern, which were parallel to the TT direction. The same testing method was applied on ED-TD plane along the TD direction. The interval between indentions was at least four times larger than the diagonal of the indenter to avoid interactions between consecutive indentations.

Microhardness test results for the heat treated AZ31B, as-extruded AM30 and as-cast AM60B are presented in Figure 4.7. The error bar with 95% confidence interval was plotted along the curve. After heat treatment, a similar microhardness profile was obtained on the RD-TD and TD-TT planes for the AZ31B sample. This suggests that the microstructure and chemical composition was homogenized after the heat treatment. It should be noted that for AM30 the microhardness observed for the ED-TT plane was slightly higher than that of the ED-TD and TD-TT planes, where there was no significant difference in microhardness between the latter two planes. This suggests that the ED-TT plane may have a slight crystallographic texture versus the other two planes, which would be consistent with the slightly elongated grains observed in Figure 4.4. However, the grain size difference through thickness did not significantly affect the microhardness. The

AM60B die-casted skin was harder than the interior because of the higher Al concentration, higher β-phase fraction and smaller grain size.

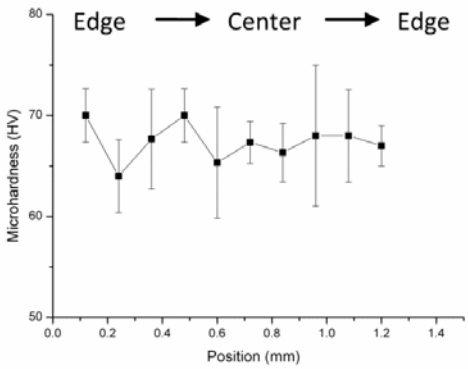

(a) Heat treated AZ31B RD-TT plane

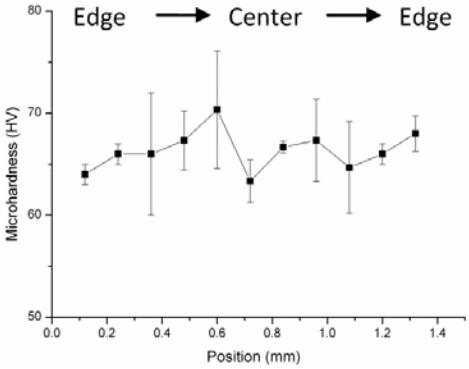

(b) Heat treated AZ31B TD-TT plane

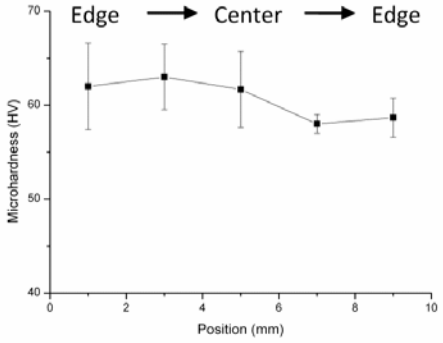

(c) As-extruded AM30 ED-TD plane

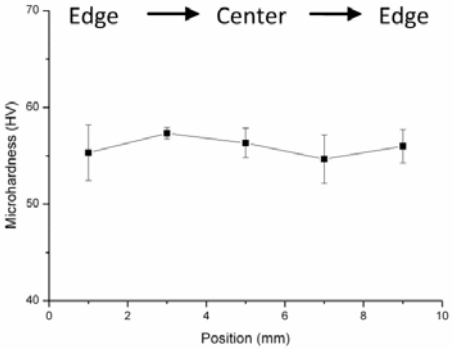

(d) As-extruded AM30 ED-TT plane

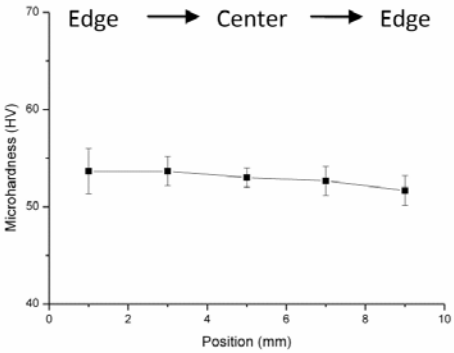

(e) As-extruded AM30 TD-TT plane

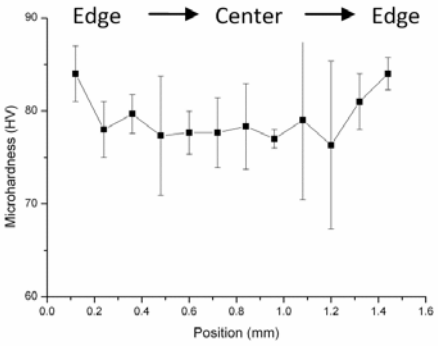

(f) As-cast AM60B cross-section

Figure 4.7 Microhardness test results.

4.1.3 XRD Texture Analysis

A texture analysis was carried out using a 2D Bruker X-Ray Diffraction (XRD) goniometer with Cu Kα radiation on the three orthogonal planes of the as-extruded AM30 specimen. A sample of AM30 was sectioned to a 1×1×1 cm cube using a precision cutting machine at 0.005 mm/s with water cooling in order to minimize cold working. Figure 4.8 defines the sample directions S1, S2 and S3. The diffracting surface remained normal to S3 for the entire test. For the ED-TD plane, the extrusion direction (ED) was aligned parallel to S2 and the transverse direction (TD) to S1; for the ED-TT plane, ED was aligned to S2 and the through thickness direction (TT) to S1; for the TD-TT plane, TT was aligned to S2 and TD to S1. Sample orientation was determined by the rotation angles ω, φ and ψ, as shown in Figure 4.8.

A 2D multiple scan was applied on each plane to cover a sufficient number of pole figure angles. Two φ scans were performed, in which φ was varied from 0° to 357.5° with a scan step of 2.5° at constant ω angle of 170° and 152°, respectively. In addition three ω scans were carried out, in which ω was varied from 132.5° to 170° with a scan step of 2.5° at constant φ of 0°, 120° and 240°, respectively. In all cases, ψ was fixed at 54.7°. The texture data was processed using GADDS software.

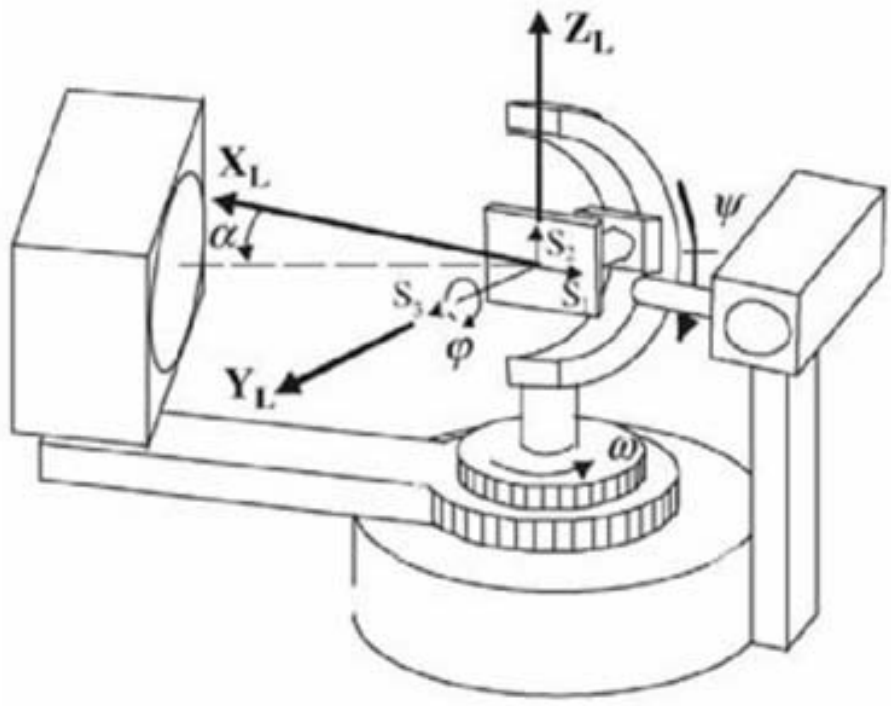

Figure 4.8 XRD diffractometer configuration [67].

4.2 Corrosion Tests

4.2.1 Sample Preparation

All samples were sectioned using a precision cutting machine at a speed of 0.005 mm/s with water cooling. The sample surface area was then measured using digital callipers. Figure 4.9 illustrates the sample preparation procedure for the electrochemical experiment. Step 1: double sided tape was placed on the test surface of the sample to stick the sample to the bottom cover of the mould. The tape was required to be large enough to cover the sample surface. Step 2: a piece of Cu tape was used to stick a Cu wire on the back of the sample. Step 3: cold-mounting epoxy was poured into a 1.25” I.D plastic

mould containing the assembly from steps 1 and 2. The samples were allowed to set for at least 8 h to ensure proper curing of the epoxy. Step 4: after removing the cold mounted samples from the mould, the double side tape was removed from the sample surface. For samples in which the alloy skin was tested, the skin surface was cleaned using acetone to remove any glue residue originating from the tape. For other samples, the surfaces were ground using 1200 grit SiC paper with ethanol (100%) as a lubricant. The samples were dried in a cold air stream immediately after the grinding process. Step 5: a conventional multi-meter was used to check electrical continuity between the wire and sample surface. To minimize experimental error, the resistance of the samples used in this study was controlled to 10 Ω or less. Step 6: a plastic straw was glued on the back of the sample to cover the wire.

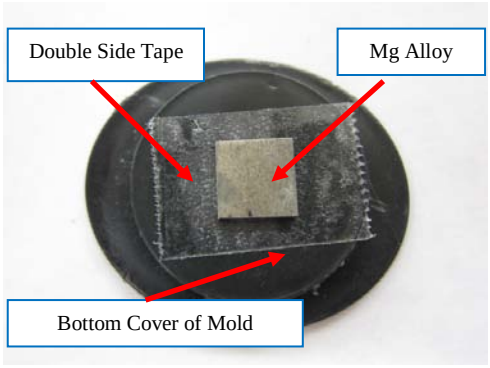

Step 1: Stick sample

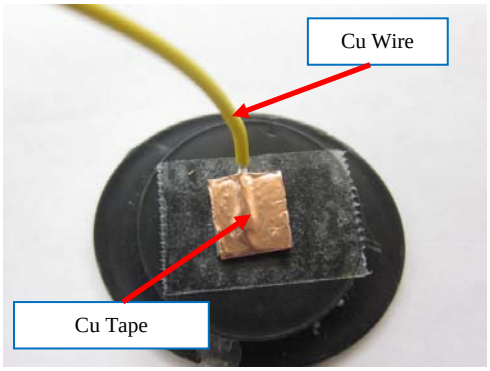

Step 2: Install wire on sample

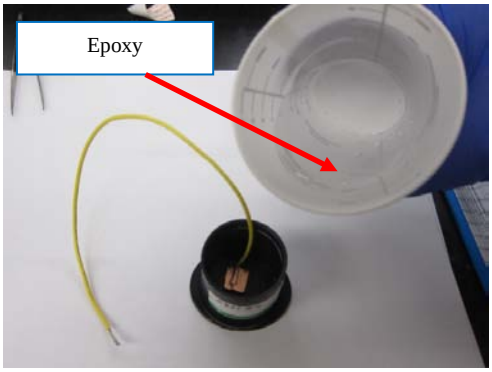

Step 3: Cold mount by using epoxy

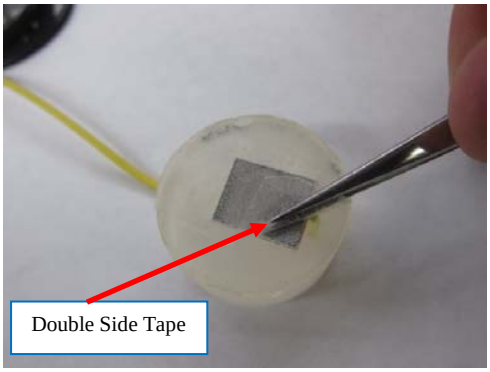

Step 4: Remove double side tape

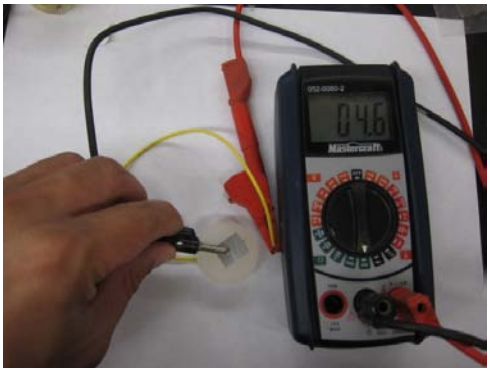

Step 5: Test electrical conductivity

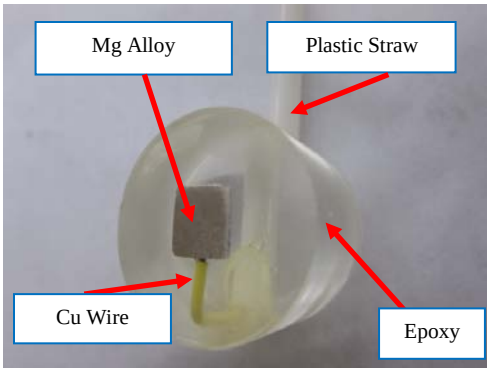

Step 6: Install plastic straw

Figure 4.9 Sample preparation procedure for electrochemical experiments.

4.2.2 Electrochemical Test Setup

A three-electrode corrosion cell which included a reference electrode (RE), working electrode (WE) and auxiliary electrode (AE), as shown in Figure 4.10, was used for all electrochemical corrosion tests. The cell had a capacity of 1000 mL. The WE, which was the test specimen, was centrally located in the test cell such that the exposed surface was facing the AE, which was a graphite rod for all experiments. A Saturated Calomel Electrode (SCE), in a salt bridge filled with saturated KCl, was used as the RE for all tests. This electrode was placed approximately 1-2 mm from the WE surface to minimize Ohmic electrolyte resistance. All electrochemical tests were conducted at room temperature using either an EG&G Princeton 273 or a GAMRY Reference 600 potentiostat. The RE was always calibrated against a standard RE in saturated KCl before testing. Any potential difference observed was used to correct the experimental data. However, if the potential difference was more than ± 20 mV, the RE was changed.

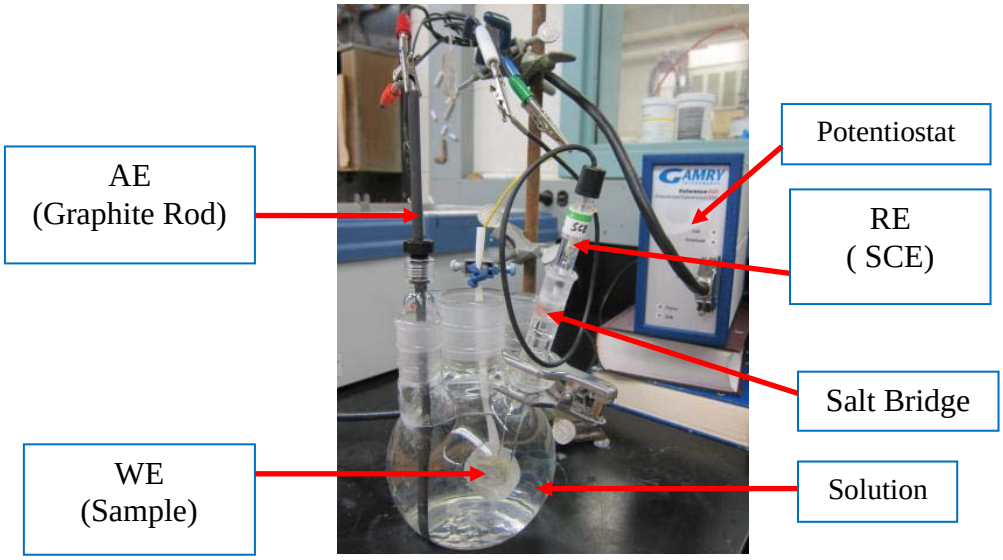

Figure 4.10 Image of electrochemical experiment set-up.

4.2.3 Cyclic Polarization Tests

To characterize the passivation breakdown and repassivation behaviour of MFERD Mg alloys, cyclic polarization tests were carried out in a mildly aggressive corrosion solution. The solution used was the cyclic salt spray solution described in the GM9540P standard. It consists of 0.9 wt % sodium chloride (NaCl), 0.1 wt % calcium chloride ($CaCl_2$) and 0.25 wt % sodium bicarbonate ($NaHCO_3$) dissolved into distill water. The as-mixed pH was approximately 7.9. The sample surface was pre-exposed to the GM9540P solution for 1 h prior to cyclic polarization testing. The E_{corr} was monitored during this exposure. Forward potentiodynamic polarization scans started at a cathodic potential of -0.25 V vs. E_{corr} and were stopped at an anodic potential of +0.5 V vs. E_{corr}. The scan was then reversed until it intersected the forward curve. The scan rate was 1 mV/s and the step size was 5 mV. This test was repeated four times for each sample. Due to the homogeneous microstructure of AZ31B after heat treatment, the AZ31B RD-TD plane was chosen for

this test. However, since the as-cast AM60B had the skin effect and the as-extruded AM30 had a weak preferred crystallographic orientation, the as-cast AM60B-AR (skin), AM60B-MP (interior) and all three planes of the as-extruded AM30 were tested.

4.2.4 Potentiostatic Test

Potentiostatic polarization tests were carried out on all alloys in the GM9540P solution to compare current density transients under different electrochemical polarization conditions. After 1 h of pre-exposure, anodic potentiostatic polarization was applied at 100 mV below E_b and 100 mV above E_b. This can ensure the tested samples in the relative passive state and in the active state, respectively. At an applied potential below E_b, all samples were held for 2 h. Because the thin AZ31B and AM60B sheet would suffer rapidly anodic dissolution at an applied potential above E_b, all samples tested in this condition were held for 0.5 h only. Cathodic potentiostatic polarization was applied at -1.8 mV_{SCE} for 2 h. This potential was chosen from the linear portion of the polarization curve used for cathodic Tafel extrapolation. At this potential, the anodic current density is insignificant related to the cathodic current density, and the cathodic process is activation controlled.

Upon completion of the anodic potentiostatic polarization tests, samples were sectioned perpendicular to the exposed surface and cold mounted using epoxy resin to compare the surface morphology. Sample mounts were prepared in a similar manner to that described in section 4.1.2.

4.2.5 Linear Potentiodynamic Polarization Test

In order to characterize the influence of crystallographic texture on the short- and long-term corrosion resistance, the ED-TD, ED-TT and TD-TT planes of the extruded AM30 bar were pre-exposed in a 0.01 M (NaCl) solution for 1 h, 3 days, 5 days and 7 days, respectively. Following this, a linear potentiodynamic polarization scan was carried out from -0.25 V to +0.5 V vs. E_{corr} using a scan rate of 0.166 mV/s.

4.2.6 Linear Polarization Resistance Tests (LPR)

The LPR test combined with the potentiodynamic polarization test was used to systematically characterize the crystallographic texture effect on electrochemical behaviour for the AM30 alloy. All tests were done in a 0.01 M (NaCl) solution. The scan started from -0.05 V to +0.05 V vs. E_{corr} using a scan rate of 1 mV/s.

The expected corrosion current density, i_{corr}, can be calculated from the measured polarization resistance (R_p) using Equations (4-1) and (4-2)

$$\log R_p = \log B - \log i_{corr} \quad (4\text{-}1)$$

Where,

$$B = \frac{\beta_a \beta_c}{2.3(\beta_a + \beta_c)} \quad (4\text{-}2)$$

is a proportionality constant. B contains approximate absolute values of the cathodic Tafel constant (β_c)= 0.12 mV/decade, and the anodic Tafel constant (β_a)= 0.12

mV/decade. These values were determined by considering the results from linear potentiodynamic polarization tests in 0.01 M (NaCl) solutions. The error in the calculated corrosion rate was negligible for different Tafel constants [68].

Chapter 5. Results

5.1 Influence of Crystallographic Orientation on the Corrosion Resistance of Extruded AM30

5.1.1 Crystallographic Texture

Figure 5.1 presents the (0002) pole figures for extruded AM30 for the ED-TD, ED-TT and TT-TD planes. It should be noted that the diffraction intensities in Figure 5.1 are plotted with the same intensity scale. The results show large radial and azimuthal distributions with a relatively high peak intensity of the basal plane for all three planes. This indicates that there was no strong preferential crystallographic orientation for either of the two extrusion surfaces, ED-TD and ED-TT, or the cross-section surface, TT-TD. However, it should be noted that the TT-TD surface (Figure 5.1(c)) did show a slightly stronger (0002) texture than was exhibited for the other planes.

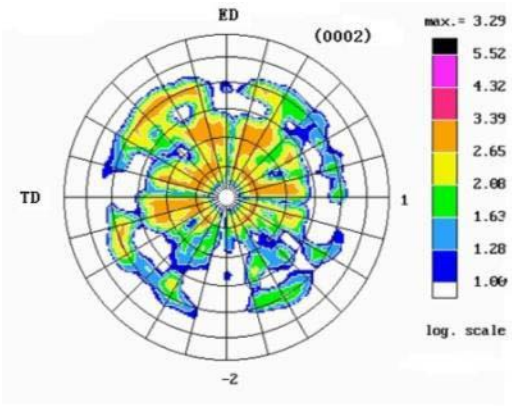

(a) ED-TD

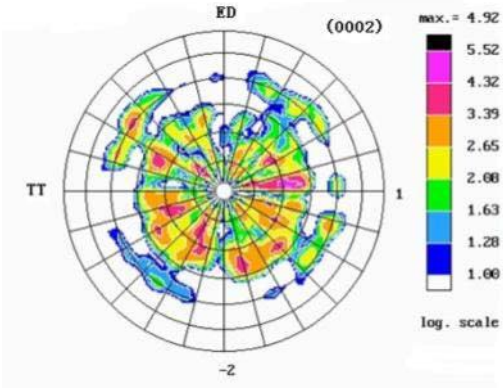

(b) ED-TT

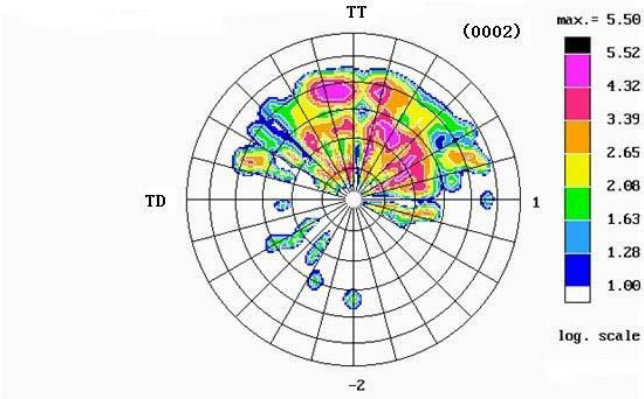

(c) TT-TD

Figure 5.1 Pole figure of extruded AM30.

5.1.2 Cyclic Potentiodynamic Polarization Test Results

Figure 5.2 shows the cyclic potentiodynamic polarization curves for AM30 for the three sample planes. These curves showed a very similar shape indicating similar cathodic and anodic polarization behaviours for these surfaces. The cathodic branches overlapped each other, attaining a similar E_{corr}. In the forward anodic polarization scans, the curves all showed passivation behaviour. The current density then dramatically increased at the critical potential, suggesting passivity breakdown. This critical potential was defined as the breakdown potential, $E_{b.}$ The reverse anodic branch followed a hysteresis loop and

intersected with the forward anodic branch at a more noble potential between E_{corr} and E_b. This potential was defined as the repassivation potential, E_{rp}.

The polarization curves did not exhibit Tafel behaviour in the anodic branch. For this reason, the cathodic Tafel extrapolation method was used to determine some critical electrochemical parameters. E_{corr}, E_b and E_{rp} were measured directly from the curves. One decade of linear cathodic current density, -50 mV versus E_{corr}, was used to extrapolate the Tafel line. The slope of this Tafel line was defined as the cathodic Tafel slope, β_c. The value of the current density at the intersection of the Tafel line and E_{corr} defined the corrosion current density, i_{corr}. The cathodic reaction was mainly the hydrogen reduction reaction. The pH of the GM9540P solution was 7.68 and, therefore, the half-cell potential for the hydrogen cathodic reaction, e_{H^+/H_2}, was calculated as -0.694 V_{SCE} using the Nernst equation. Further extrapolation of the cathodic Tafel line to e_{H^+/H_2}, defined the cathodic exchange current density, $i_{o,c}$.

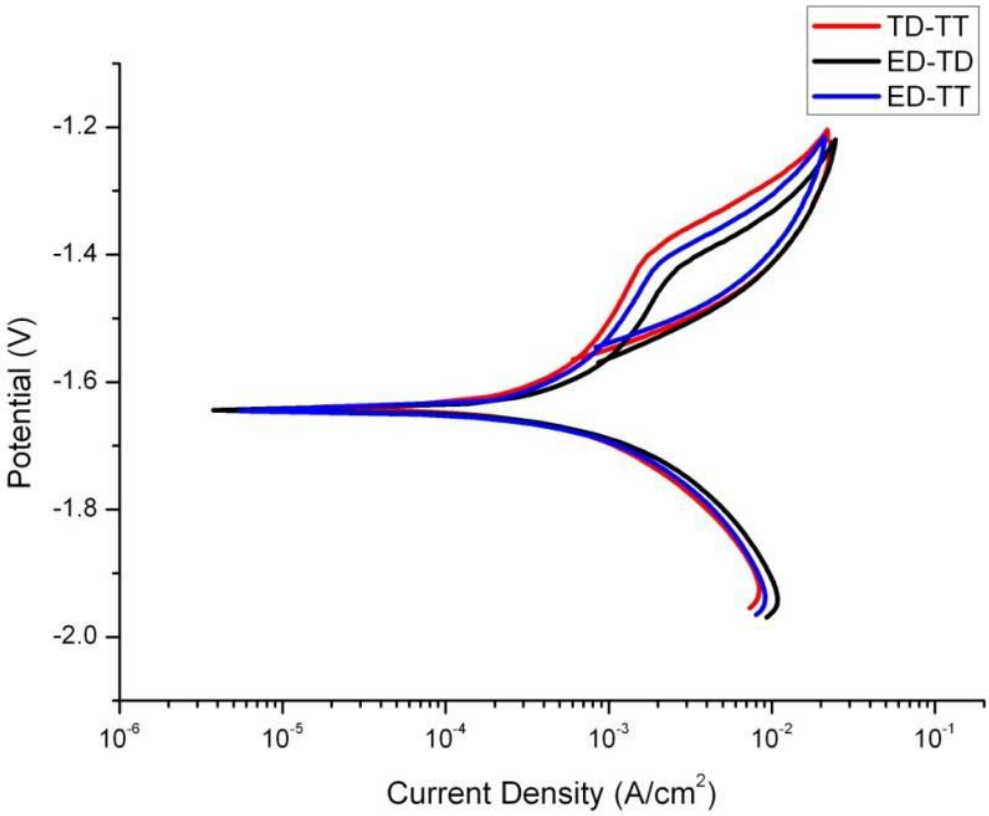

Figure 5.2 Cyclic polarization curves of AM30 for the different extrusion planes in the GM9540P solution.

For each plane, all cyclic polarization tests were repeated four times. The average values of these electrochemical parameters from these repeated experiments are shown in Table 5.1. An inspection of Table 5.1 will show that the electrochemical parameters were similar to each other considering experimental error and errors associated with the manual Tafel extrapolation. For example, the maximum difference for E_{corr}, E_b and E_{rp} were 20 mV_{SCE}, 10 mV_{SCE}, and 20 mV_{SCE}, respectively. Due to the scan step size of 5 mV, these differences are considered to be negligible. From this data, it can be concluded that the three sample planes exhibited the same corrosion, passivity breakdown and repassivation behaviours. For example, the E_b were approximately 240 mV more noble than the E_{corr}

for all sample planes. Also, the E_{rp} were approximately 110 mV more noble than E_{corr} and 120mV more negative than E_b for all sample planes. This suggests that no pitting occurred on the three AM30 planes after one hour immersion under the Open Circuit Potential (OCP) condition. Corrosion current densities measured on all exposed planes were within the same order of magnitude. This suggests that they corroded at the same rate in this solution. Additionally, the same order of magnitude for the cathodic exchange current density indicates a similar hydrogen evolution rate. These two kinetic parameters tend to confirm that there was no significant difference of corrosion resistance between the AM30 extrusion planes.

Table 5.1 Electrochemical Parameters Extrapolated from Cyclic Polarization Test in GM9540P Solution at Room Temperature for the Three Extruded AM30 Planes.

Plane	**E_{corr} (V_{SCE})**	**E_b (V_{SCE})**	**E_r (V_{SCE})**	**β_c (V/dec.)**	**i_{corr} (A/cm^2)**	**$i_{o,c}$ (A/cm^2)**
ED-TD	-1.66	-1.42	-1.54	0.213	10.2×10^{-4}	8.8×10^{-9}
ED-TT	-1.64	-1.41	-1.53	0.213	8.6×10^{-4}	6.7×10^{-9}
TD-TT	-1.66	-1.41	-1.55	0.205	9.3×10^{-4}	1.9×10^{-9}

5.1.3 Anodic Potentiostatic Test Results

Figure 5.3 presents the anodic current density transient recorded for a constant applied potential 100mV above E_b and below E_b, respectively, for the three planes of extruded AM30 in the GM9540P solution. At the applied potential 100mV below E_b, the initial anodic current density for each plane increased rapidly. After reaching a maximum value, the current density exhibited a sharp decrease which then decayed at a very slow rate. The current density of each plane measured at steady state was within the same order of magnitude for all sample planes. However, at the applied potential 100mV above E_b, the current density increased rapidly until it attained a plateau value. The steady state current density for each plane was within one order of magnitude. For all sample planes, the anodic current density at the applied potential 100mV above E_b was at least one order of magnitude higher than that at the applied potential below E_b.

Figure 5.4 shows the surface morphology after anodic potentiostatic tests in the GM9540P solution. At the applied potential 100mV below E_b, the surface was dull

compared to the initial surface but still smooth. This indicates that no localized corrosion occurred. By contrast, at the applied potential 100mV above E_b, a rough surface was observed on each plane which suggests that localized corrosion occurred. Figure 5.5 presents a cross-sectional view of the surface morphology at higher magnification. The localized corrosion damage seems to have spread widely throughout the overall surface instead of penetrating deeply. This suggests that the same corrosion mode was observed on the three planes under the same test conditions. At the applied potential 100mV below E_b, the surface was very smooth and covered with a film. This film was not evenly distributed and contained some defect sites. This may be a result of drying process after removing the samples from the aqueous solution. Although the film exhibited some defect sites, it still provided protection compared to the bare substrate directly exposed to the corrosive environment. In contrast, at the applied potential 100mV above E_b, pitting attack was observed on all sample planes.

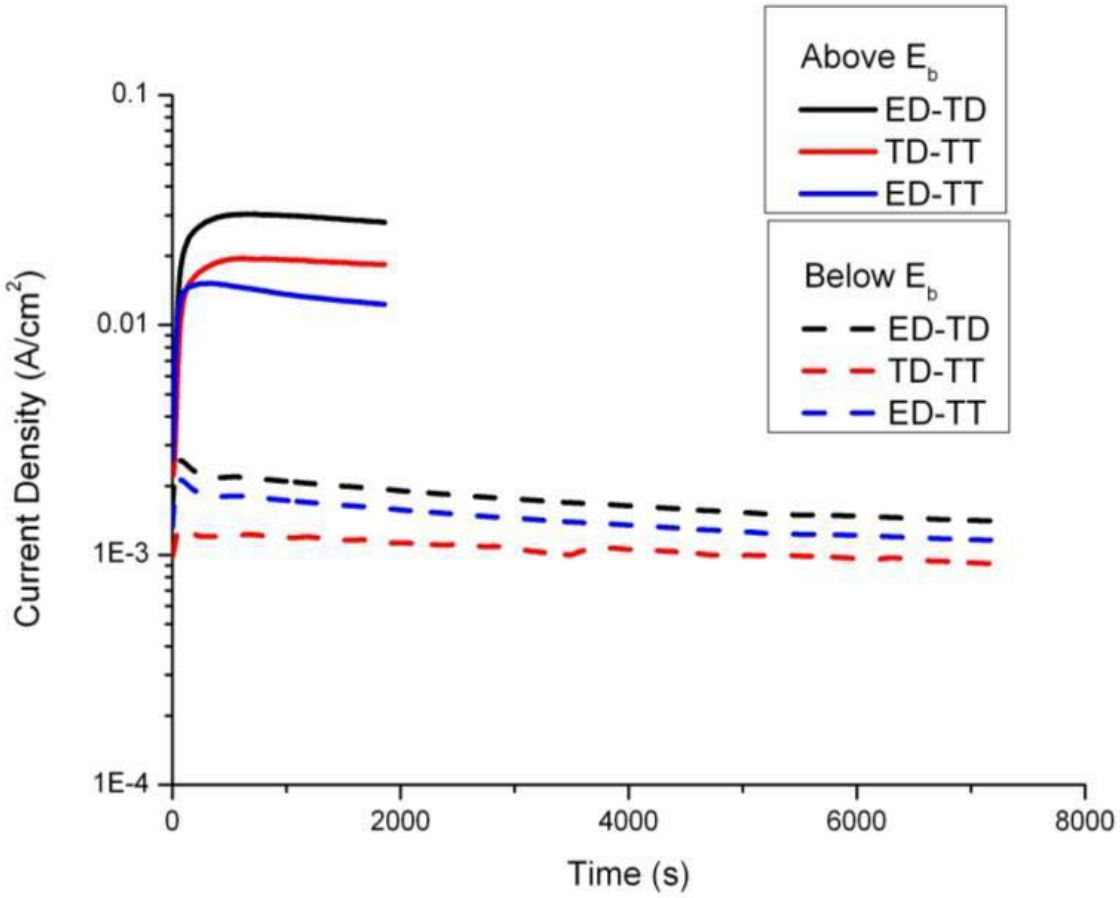

Figure 5.3 Anodic current density transient in GM9540P solution at an applied potential 100mV below E_b and above E_b on the three AM30 extrusion planes.

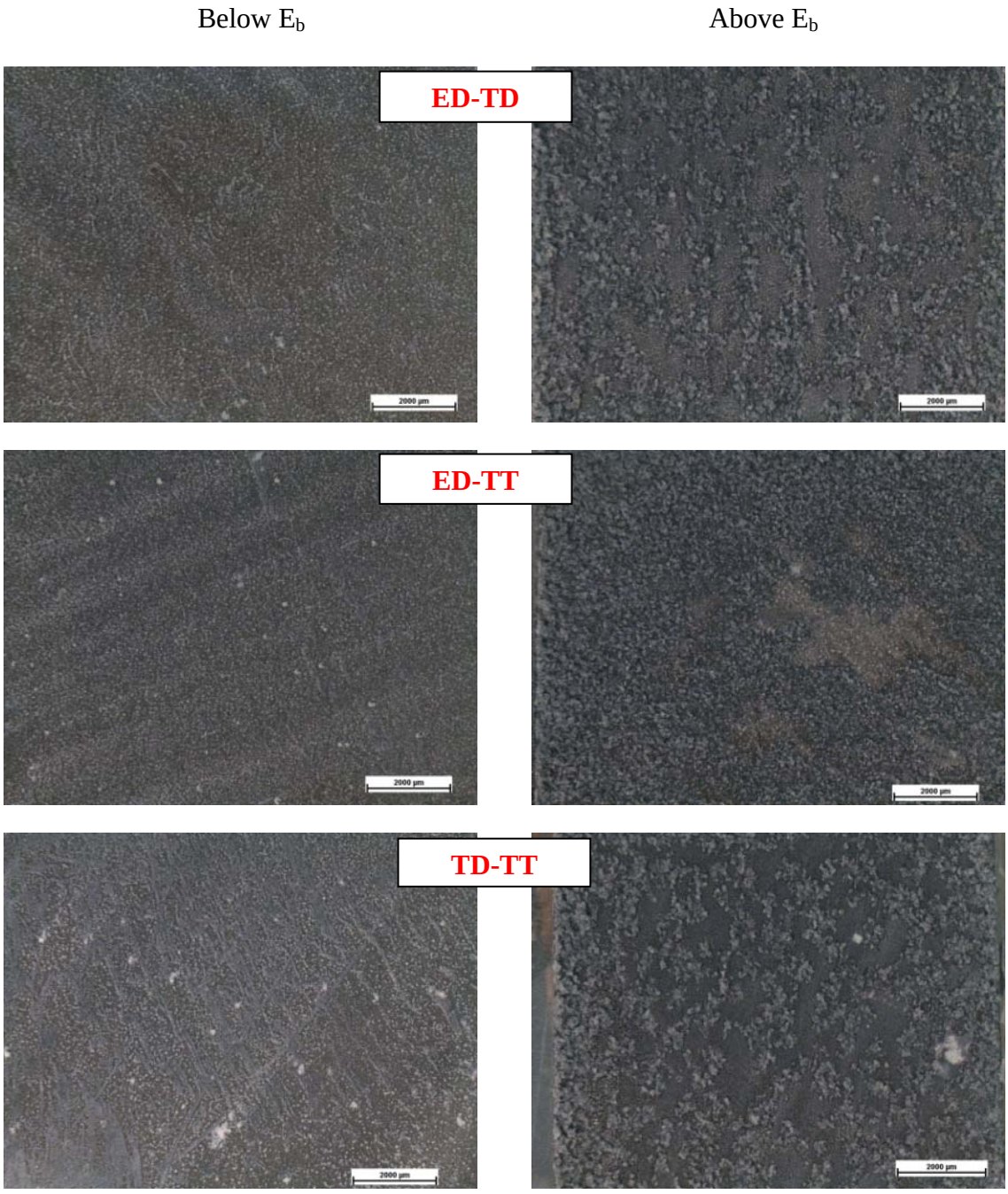

Figure 5.4 Surface morphology of AM30 after anodic potentiostatic tests at an applied potential 100mV below and above E_b in room temperature GM9540P solution.

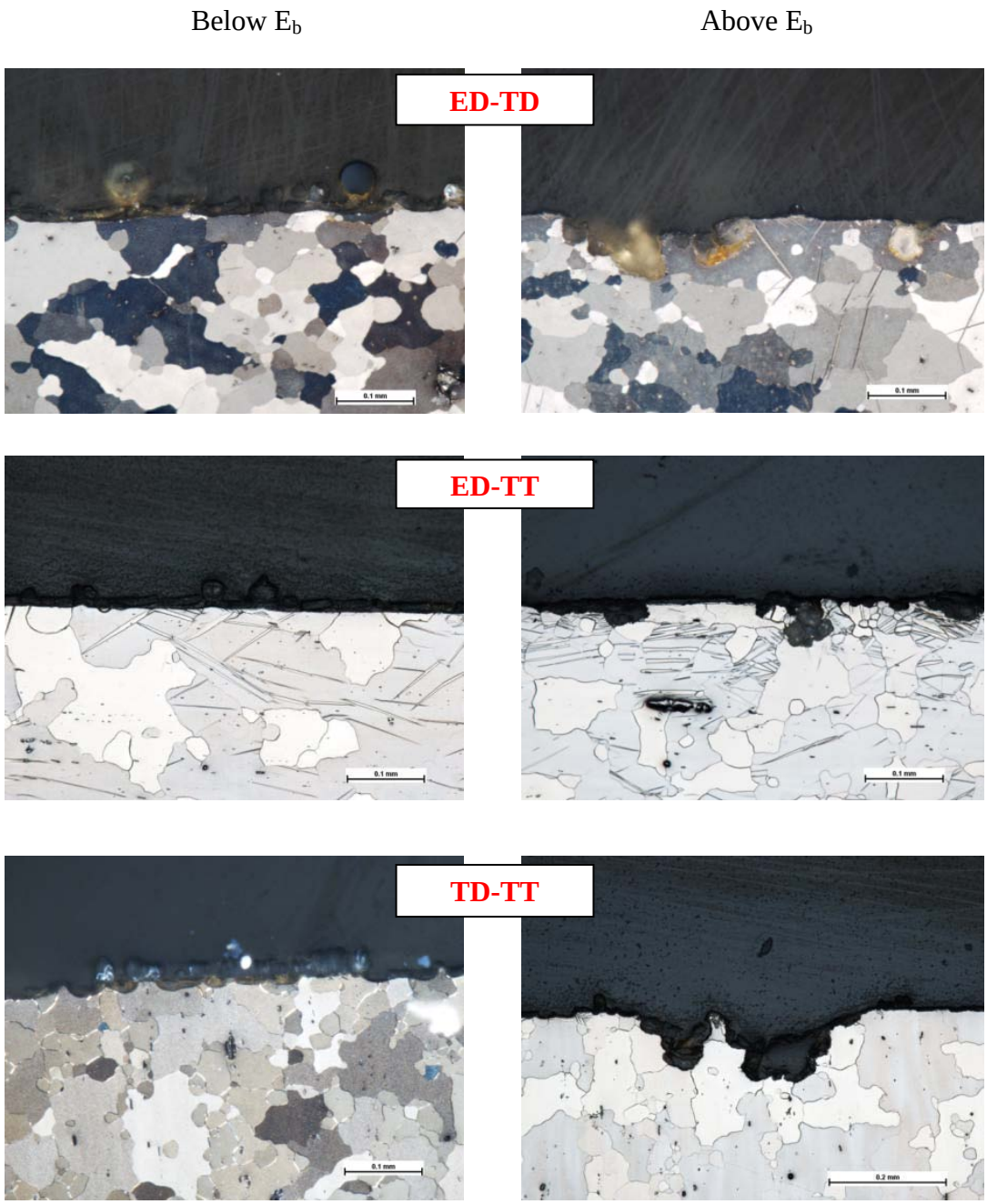

Figure 5.5 Light optical microscopy images of sample surfaces of AM30, in cross-section view, after anodic potentiostatic test at an applied potential 100mV below and above E_b in room temperature GM9540P solution.

5.1.4 Influence of Exposure Time Results

Figure 5.6 shows the linear potentiodynamic polarization tests performed on the three planes of AM30 after immersion in 0.01 M NaCl solution for 3, 5 and 7 days, respectively. To compare with the short term corrosion behaviour, the three planes were also tested after 1 hour immersion in the same solution under the same experimental conditions. The three planes exhibited similar general anodic and cathodic polarization behaviour. This was evident from the sharp anodic passivity breakdown behaviour above E_{corr} and the overlapping cathodic branches with similar cathodic Tafel slopes exhibited by all samples. The anodic E_b observed on the polarization curves after a 1 hour immersion were more difficult to determine due to the relatively smooth curvature compared with those measured after long term immersion. The E_b for the 1 hour immersion tests was determined by finding the highest current density change after the linear region. The results suggest that the passive film formed on AM30 after 1 hour immersion was less stable compared with that after long term immersion (3, 5, 7 days). For the same immersion time, the E_{corr} exhibited for all three planes were similar, except the ED-TD plane after immersion for 7 days, which showed a slightly higher E_{corr} than the other two planes. This may have been caused by the low electric conductivity of the 0.01 M NaCl solution.

Table 5.2 shows the electrochemical parameters extrapolated from the linear potentiodynamic polarization tests using the same cathodic Tafel extrapolation method as described in Section 5.1.1. The cathodic exchange current density was measured at the

hydrogen half cell potential e_{H^+/H_2} which was -0.654 V_{SCE} in a solution with a pH of 7. In general, all the parameters for long term immersion (3 days, 5 days, 7 days) were similar for each plane and exposure time. However, the parameters were approximately 100 mV more noble than the average E_{corr}, 100 mV more noble than the average E_b and 10 times less than the average corrosion rate as compared to those for the short term pre-exposed (1 hour) surfaces. In addition, the hydrogen cathodic reaction exchange current density for each test was within one order of magnitude. Given the same immersion time, each plane showed similar corrosion resistance. The E_{corr} and E_b for the three planes varied by less than 50 mV, the corrosion rates were within one order of magnitude and the cathodic current densities were within two orders of magnitude for all samples. Moreover, the group of samples subjected to immersion for 5 days showed a maximum difference of 90 mV in E_b and the ED-TD plane immersed for 7 days had an E_{corr} 40 mV higher than the other two planes. The overall trend provides evidence that these differences could be attributed to experimental error.

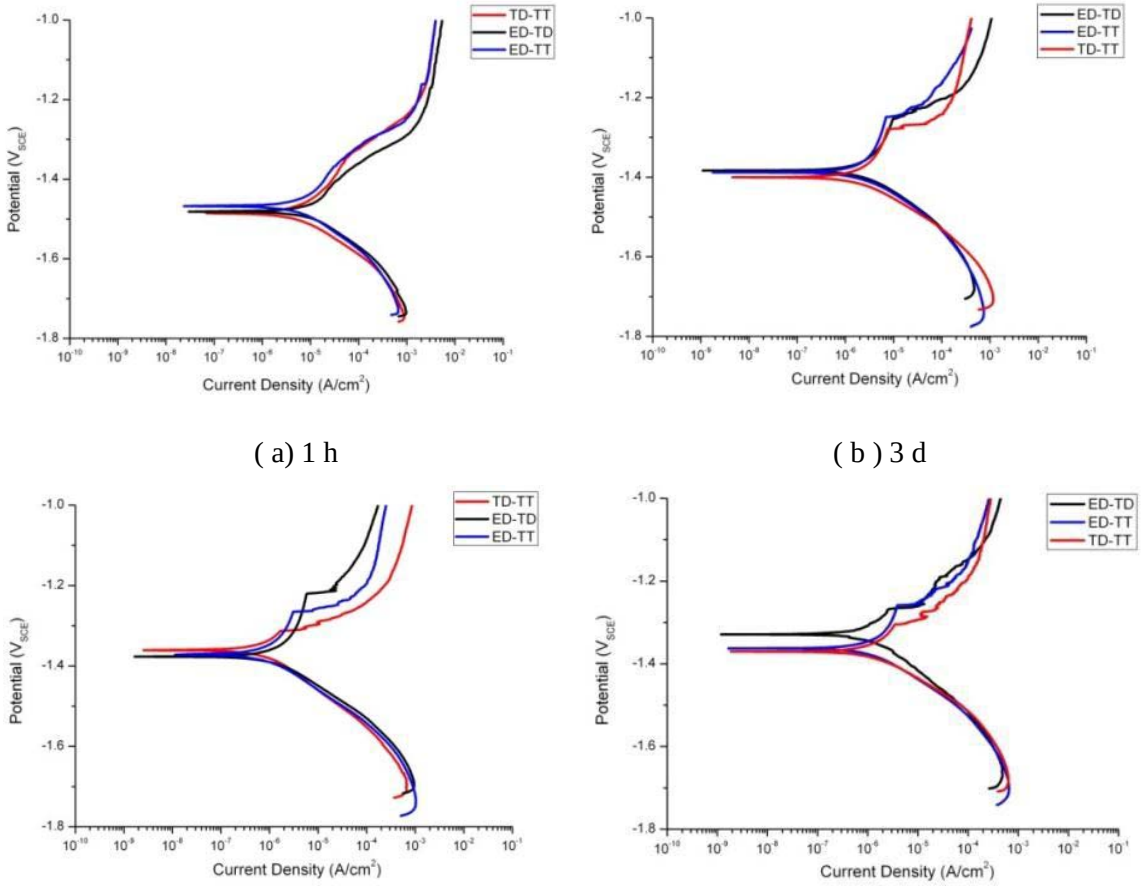

Figure 5.6 Linear potentiodynamic polarization curves for AM30 three planes after (a) 1 h, (b) 3 d, (c) 5 d, (d) 7 d immersion in room temperature 0.01 M NaCl solution.

Table 5.2 Electrochemical Parameters Extrapolated from Linear Potentiodynamic Polarization Tests in Room Temperature 0.01 M NaCl Solution for Extruded AM30 Pre-Exposed for 1 h, 3 d, 5 d and 7 d.

Pre-expose Time	**Plane**	**E_{corr} (V_{SCE})**	**E_b (V_{SCE})**	**β_c (V/dec.)**	**i_{corr} (A/cm^2)**	**$i_{o,c}$ (A/cm^2)**
1 h	ED-TD	-1.48	-1.40	0.095	18.3×10^{-6}	4.4×10^{-16}
	ED-TT	-1.46	-1.36	0.092	11.7×10^{-6}	1.9×10^{-16}
	TD-TT	-1.48	-1.34	0.094	13.0×10^{-6}	2.2×10^{-6}
3 d	ED-TD	-1.38	-1.25	0.089	2.4×10^{-6}	1.5×10^{-16}
	ED-TT	-1.39	-1.25	0.089	2.8×10^{-6}	1.3×10^{-16}
	TD-TT	-1.40	-1.27	0.086	2.6×10^{-6}	0.6×10^{-16}
5 d	ED-TD	-1.37	-1.22	0.089	2.1×10^{-6}	1.8×10^{-16}
	ED-TT	-1.37	-1.27	0.088	1.6×10^{-6}	1.3×10^{-16}
	TD-TT	-1.36	-1.31	0.089	1.3×10^{-6}	2.9×10^{-16}
7 d	ED-TD	-1.33	-1.27	0.091	1.1×10^{-6}	4.1×10^{-16}
	ED-TT	-1.36	-1.26	0.088	1.5×10^{-6}	1.4×10^{-16}
	TD-TT	-1.37	-1.30	0.089	1.7×10^{-6}	1.0×10^{-16}

Figure 5.7 shows the results of the linear polarization resistance test for the three AM30 planes in the 0.01 M NaCl solution. The E_{corr} and polarization resistance were measured after 1, 4, 5, 6, 7 and 8 days, respectively. The corrosion rate was calculated using polarization resistance and the estimated Tafel constants, as described in Section 4.2.6. For these three planes, there was no significant difference between the corrosion

resistances for eight days because the maximum difference of E_{corr} measured at the same pre-exposed period was within 50 mV and the corrosion rates were within one order of magnitude. These results were consistent with the linear potential dynamic polarization test in the 0.01 M NaCl solution and the cyclic potentiodynamic test in the GM9540P solution.

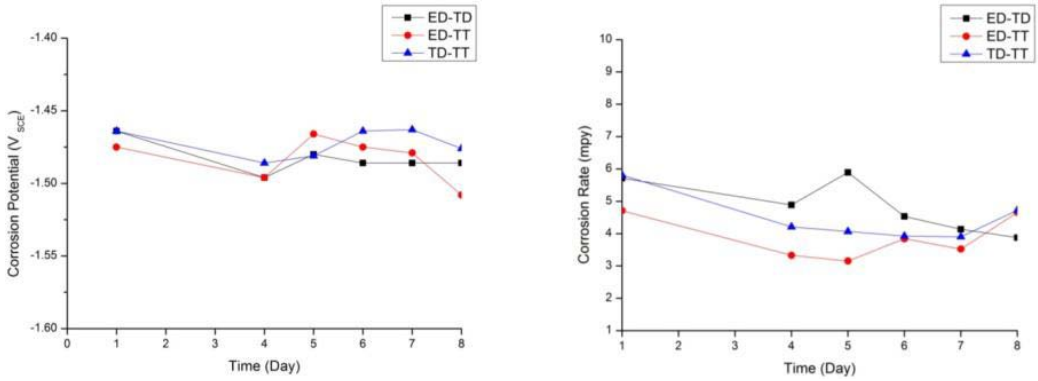

(a) The dependence of measured E_{corr}

(b) The dependence of calculated corrosion rate

Figure 5.7 Liner polarization resistance test on extruded AM30 planes in 0.01 M NaCl solution at room temperature as a function of time.

5.2 Relative Corrosion Behaviour of Mg-Al Alloys

5.2.1 Cyclic Potential Test Results

The as-received skin surface (AR) for the extruded AM30 and die-cast AM60B were carefully conserved to compare their microstructures with those of their interior. The interior was exposed by mechanical polishing (MP) to remove the skin layer. AZ31B after heat treatment showed no differences in microstructure between the skin and

interior. Thus, only the MP surface of AZ31B was tested to compare with the other Mg alloys.

Figure 5.8 shows the cyclic potentiodynamic polarization curves for the MFERD alloys measured in the GM9540P solution at room temperature after one hour of immersion. In general, all exposed surfaces showed anodic passivity breakdown and repassivation behaviour in this solution. This was recognized as the previously discussed E_b above E_{corr} and the hysteresis loop of the reverse anodic polarization branch. Although the AM30 skin layer contained coarse grains, the shape of its anodic and cathodic polarization curves did not show a significant difference with its interior as shown in Figure 5.8(a). Both the AR and MP surfaces exhibited similar E_{corr}, E_b and E_{rp}. However, the AM60B skin showed a remarkable difference in anodic cyclic polarization behaviour versus its interior as shown in Figure 5.8(b). The AM60B skin displayed a higher E_{corr} and lower anodic current density just below E_b compared with its interior. After reaching the same E_b, both AR and MP surfaces exhibited the same forward and reverse anodic polarization behaviour and ended at the same E_{rp}. The E_{rp} of the AR surface was the same as its E_{corr}, while the E_{rp} of the MP surface was below its E_{corr}. Cyclic polarization curves of the MP surfaces for AZ31B, AM30 and AM60B are compared in Figure 5.8(c). AM30 and AZ31B showed approximately the same polarization behaviour, which was in turn significantly different from the behaviour of AM60B. Significantly higher anodic current densities were observed for both AM30 and AZ31B compared with that of AM60B. Furthermore, both the E_b and E_{rp} of AM30 and AZ31B were above their E_{corr}, whereas

AM60B showed similar E_{rp} and E_{corr}. Nevertheless, all MP surfaces of AM30, AZ31B and AM60B exhibited similar E_b and E_{rp}.

Table 5.3 presents the electrochemical parameters extrapolated from Figure 5.8 using the same cathodic Tafel extrapolation method as described in section 5.1.1. AM60B-MP had an E_{corr} 100 mV more noble and a corrosion current density one order of magnitude less than both AM30-MP and AZ31B-MP, which exhibited similar E_{corr} and corrosion current densities. The maximum difference of E_b measured for AZ31B-MP, AM30-MP and AM60B-MP was 30 mV, which is negligible. The cathodic exchange current density exhibited on each surface condition was within a factor of 3.6, with the exception of AM60B-AR, which had a cathodic exchange current density a factor of 6.4 lower than AM60B-MP. There was no significant difference in the parameters for the MP and AR surfaces of AM30. However, the AM60B skin showed an E_{corr} 60 mV more noble and lower cathodic Tafel slope than its interior.

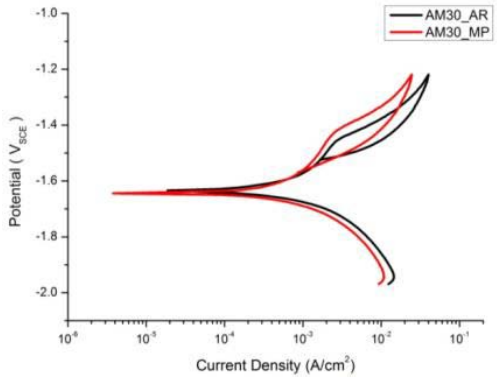

(a) MP and AR surface of AM30

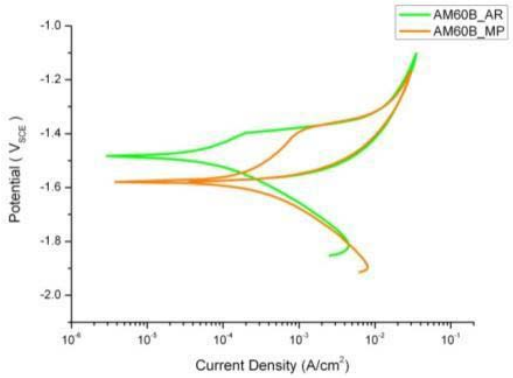

(b) MP and AR surface of AM60B

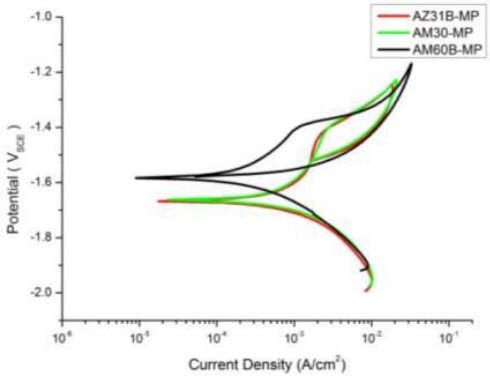

(c) MP surface of AZ31B, AM30, AM60B

Figure 5.8 Cyclic potentiodynamic polarization curves for MP and AR surface of (a) AM30, (b) AM60B and (c) MP surface of AZ31B, AM30, AM60B. Experiments were done in room temperature GM9540P solution after 1 h immersion.

Table 5.3 Electrochemical Parameters Extrapolated from Cyclic Potentiodynamic Polarization Test in Room Temperature GM9540P Solution.

Alloy	**E_{corr} (V_{SCE})**	**E_b (V_{SCE})**	**E_r (V_{SCE})**	**β_c (V/dec.)**	**i_{corr} (A/cm^2)**	**$i_{o,c}$ (A/cm^2)**
AM30-AR	-1.63	-1.46	-1.52	0.202	10.7×10^{-4}	22.8×10^{-9}
AM30-MP	-1.66	-1.42	-1.54	0.213	10.2×10^{-4}	11.6×10^{-9}
AZ31B-MP	-1.66	-1.43	-1.52	0.215	11.4×10^{-4}	24.7×10^{-9}
AM60B-AR	-1.50	-1.41	-1.57	0.180	1.6×10^{-4}	5.8×10^{-9}
AM60B-MP	-1.56	-1.40	-1.58	0.218	3.7×10^{-4}	41.2×10^{-9}

5.2.2 Anodic Potentiostatic Test Results

Figure 5.9 illustrates the anodic current density transit for the MP surface of AZ31B, AM30, AM60B and the AR surface of AM60B in GM9540P solution at room temperature at an applied potential 100mV above E_b and below E_b, respectively. Due to the negligible difference of anodic polarization behaviour between AM30-AR and AM30-MP, the anodic potentiostatic test was not applied to AM30-AR. Moreover, no test was applied to the AM60B-AR surface at an applied potential 100mV below E_b because there was only a 90 mV difference between E_b and E_{corr} for AM60B-AR.

At the applied potential 100mV below E_b, the initial anodic current density for each plane increased rapidly. After reaching a maximum value, the current density exhibited a sharp decrease and then reached a plateau. However, at an applied potential 100mV above E_b, the current density increased rapidly to a steady state value. The current density measured

at an applied potential 100mV above E_b for each alloy was at least one order of magnitude higher than that measured at an applied potential 100mV below E_b. It should be noted that AM60B-MP displayed a lower current density than AZ31B-MP and AM30-MP for applied potentials 100mV above and below E_b.

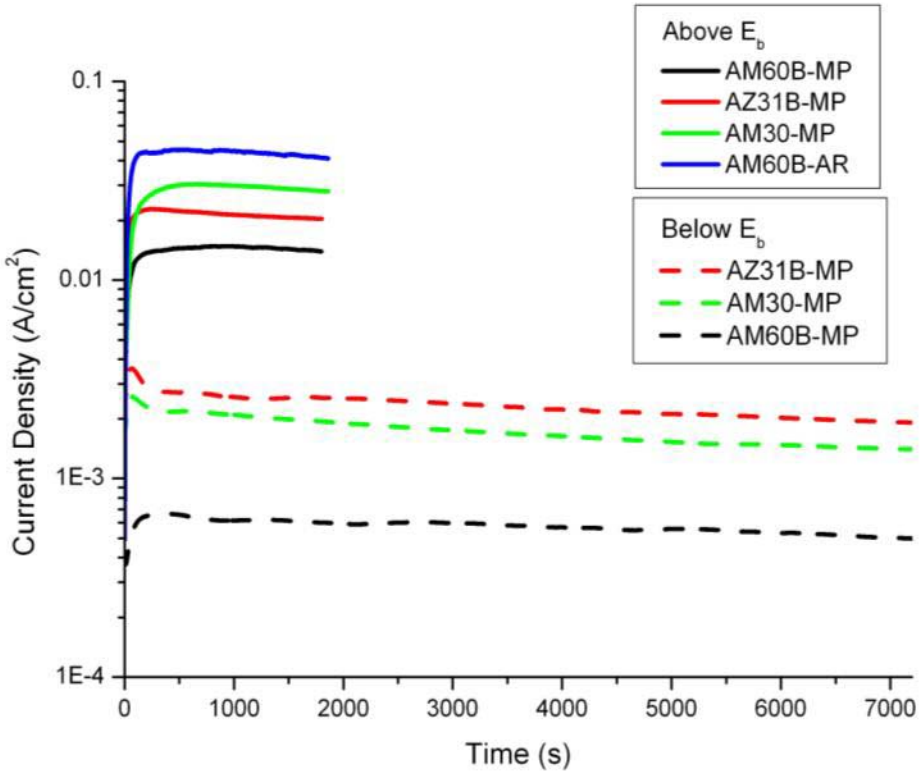

Figure 5.9 Anodic current density transit for MP surface of AZ31B, AM30, AM60B and for AR surface of AM60B in GM9540P solution at room temperature for applied potential 100mV above and below E_b.

Figure 5.10 compares the surface morphology after the anodic potentiostatic tests in room temperature GM9540P solution. At an applied potential 100mV below E_b, the surface was dull but macroscopically smooth. This indicates that no localized corrosion occurred. By

contrast, at an applied potential 100mV above E_b, a rough surface was observed for all exposed surfaces, which suggests that localized corrosion occurred on these surfaces. In addition, this localized corrosion damage seemed to spread widely throughout the overall surface instead of penetrating deeply.

Figure 5.11 presents cross-sectional images of the surface morphology. At an applied potential 100mV below E_b, the surface was smooth. However, at an applied potential 100mV above E_b, pitting attack was observed on all alloys.

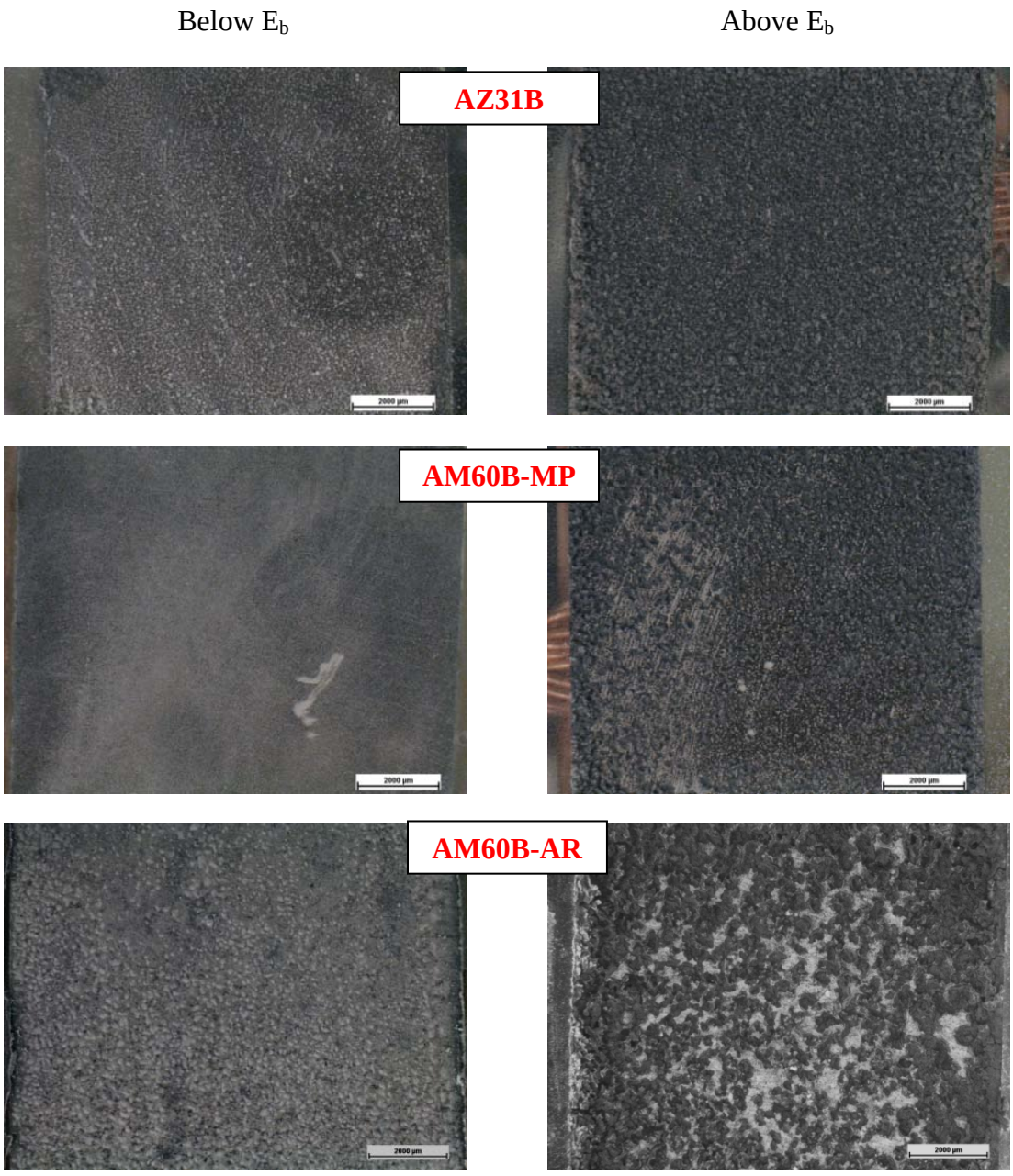

Figure 5.10 Surface morphology after anodic potentiostatic tests at applied potential 100mV below and above E_b in room temperature GM9540P solution.

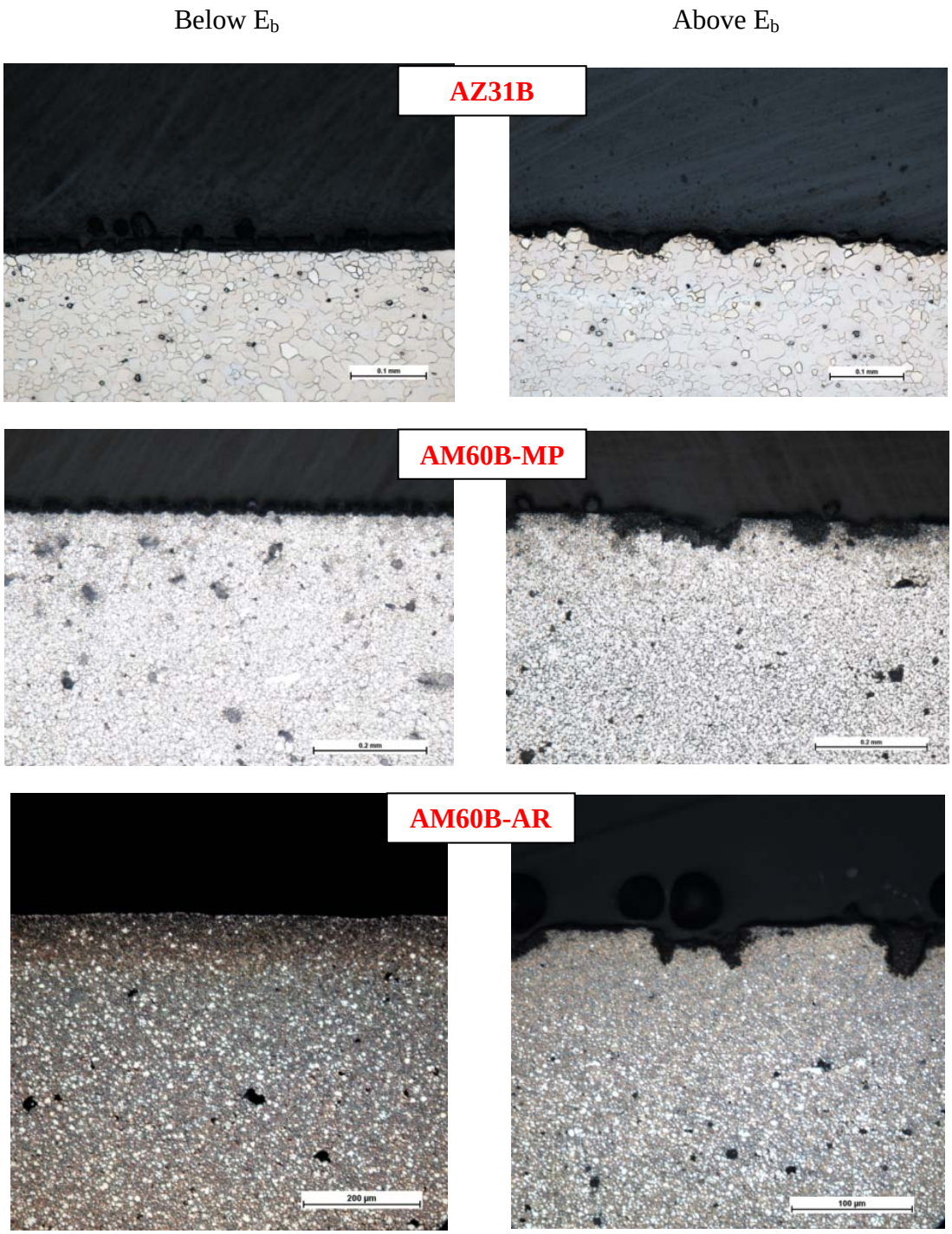

Figure 5.11 Light optical microscopy images of surface, in cross-section view, after anodic potentiostatic test 100mV below and above E_b in room temperature GM9540P solution.

5.2.3 Cathodic Potentiostatic Test Results

Figure 5.12 shows the cathodic current density transient for the MP surfaces of the three experimental Mg alloys and the AR surface of AM60B at -1.80 V_{SCE} in room temperature GM9540P solution. The cathodic current density transient curve of AM60B-AR showed a slight decay after rapidly reaching its maximum value in the initial stage. The remaining alloy surfaces showed a smooth transition curve from the rapidly increasing initial stage to a steady state value. The final constant current densities exhibited on all alloy surfaces were within the same order of magnitude.

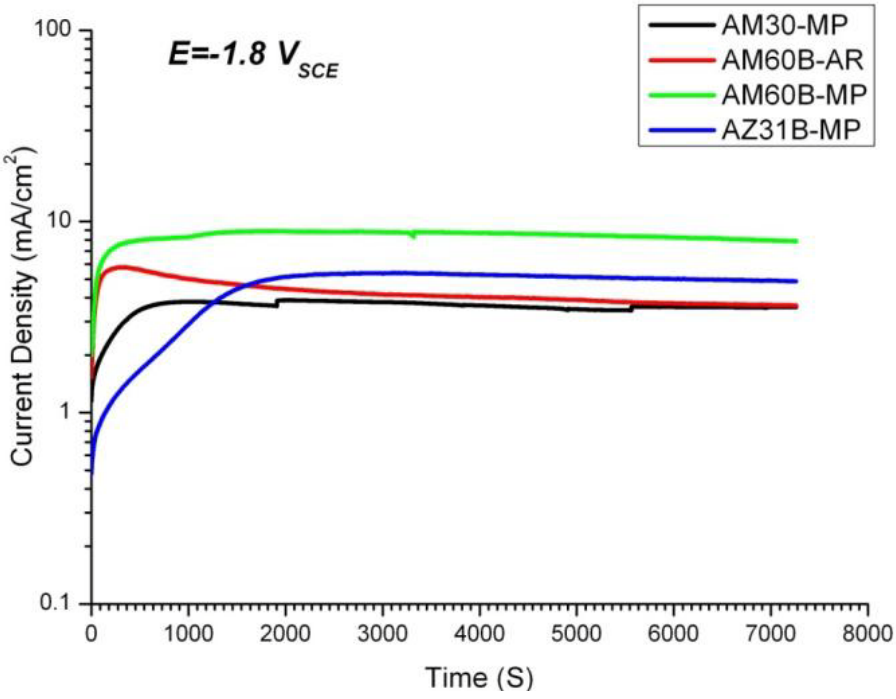

Figure 5.12 Cathodic current density transient at -1.80 V_{SCE} in room temperature GM9540P solution.

Chapter 6. Discussion

6.1 Comparative Corrosion Behaviour of Mg-Al Alloys

The first significant finding of this research is that all of the MFERD magnesium alloys studied exhibited similar breakdown potentials (E_b) above the corrosion potential (E_{corr}) in room temperature GM9540P solution after aging 1 hour, regardless of differences in alloy chemical composition or microstructure. This is shown in Figure 5.8 and Table 5.3, suggesting that the corrosion behaviour of all the MFERD alloys transitioned from a state of partial passivation to a state of localized corrosion at the same applied potential. A summary and discussion of the corrosion mechanisms at applied potentials 100 mV below E_b and above E_b will be presented below to elucidate the influence of microstructural parameters (e,g, α-phase, β-phase, Al-Mn intermetallic particles, skin effect) and environmental factors (solution concentration, applied potential) on MFERD magnesium alloy corrosion resistance.

6.1.1 Corrosion Behaviour Below E_b

At an applied potential 100 mV below E_b, the corrosion morphology was relatively smooth, without any significant localized corrosion attack (Figure 5.4, Figure 5.5 and Figure 5.11). This indicates that the alloys were protected by a surface film. It has been widely reported that this surface film contains defects and only provides limited protection to the substrate [6-7, 15, 49, 57-58, 61].

A comparison of the corrosion current density (i_{corr}) extracted from the potentiodynamic polarization curves at E_{corr} (Table 5.3) suggests that there was a meaningful difference between the corrosion resistance of the three Mg alloys. In this study the cathodic Tafel slope was determined manually using the cathodic polarization curve, i.e. 50 mV below E_{corr} with one decade of current density range. It is recognized that using this method introduces an error in the value of the extrapolated i_{corr} by a factor of 5 to 10 [47]. Further extrapolation of the cathodic Tafel line to the cathodic half-cell potential will amplify the error due to the logarithmic nature of the current density axis. Thus, a difference in i_{corr} and $i_{o,c}$ within one order of magnitude is likely insignificant. Although AM60B-MP had an i_{corr} of a factor of 3 less than AZ31B-MP and AM30-MP, the anodic potentiostatic plots at -100 mV vs E_b indicate that AM60B-MP indeed exhibited a lower anodic dissolution rate than AZ31B-MP and AM30-MP (Figure 5.9). This gives confidence to claim that the AM60B-MP surface had a better corrosion resistance than AZ31B-MP and AM30-MP. By contrast, there was no significant differences in the i_{corr} and anodic potentiostatic plots were observed for AZ31B-MP and AM30-MP. Thus, the relative ranking of corrosion resistance for the MP surfaces, at E_{corr}, in room temperature GM9540P solution is given by:

$$\text{AM60B} > \text{AM30} \approx \text{AZ31B}$$

This ranking agrees with the claim that increasing alloy Al content reduces the corrosion rate of Mg-Al alloys [15, 24, 42, 49, 56, 58]. In addition, it confirms the argument that an alloy Zn content of less than 3 wt % does not significantly affect the corrosion rate of Mg-Al alloys [50, 60].

The magnesium cathodic half-cell reaction is hydrogen evolution. It is believed that this cathodic process occurs at the interface between the film and the solution rather than on the metallic substrate [23-24]. Due to the n-type semiconducting properties of the surface film formed on Mg alloys [49, 69], it contains excess negative charge carriers which results in easy electron transfer through the surface film to react with protons in the solution [24, 42]. The cathodic exchange current density ($i_{o,c}$), a fundamental kinetic parameter, is strongly affected by the nature of the surface on which the hydrogen evolution reaction occurs. In this study, all MP surfaces exhibited an $i_{o,c}$ within one order of magnitude and similar cathodic Tafel constants (β_c, Table 5.3). In addition, the similar steady state cathodic current density (Figure 5.12) confirmed that all MP surface exhibited similar cathodic kinetics. This suggests that the outer layer of the surface films formed on these Mg alloys was of similar chemical composition and structure.

Recent research on the surface film formed on Mg-Al alloys in a mildly aggressive solution shows that it comprises two layers [15, 18]. The outer layer of the surface film is formed by a precipitation reaction [15] and is largely composed of $Mg(OH)_2$-$MgCO_3$ with a low Al/Mg ratio [18] . The inner layer of the surface film is the native film formed due to atmospheric exposure [15] and mainly consists of MgO-$Mg(OH)_2$ with a high Al/Mg ratio [15, 18]. As shown above, the presence of the β-phase in AM60B (Figure 4.7) and the 1 wt % solute (Zn) content difference between AZ31B and AM30 (Table 4.1) did not strongly affect the electrochemical properties of the outer surface layer in the present

study (Table 5.3). For this reason, the cathodic reaction was independent of any substrate metallurgical factors. The cathodic steady-state current density transients exhibited by all exposed MP surfaces were similar at the applied potential of -1.8 V_{SCE} (Figure 5.12). This confirms that the microstructure of Mg alloys did not have a significant influence on cathodic kinetics. However, the AM60B-MP surface exhibited a higher E_{corr} than that measured for either AZ31B-MP or AM30-MP (Table 5.3). According to the Nernst equation, the open circuit cathodic half-cell potential, $e_{o,c}$, should be the same because the samples were tested in the same solution (pH is constant). A more positive E_{corr} will reduce the cathodic current density due to the reduced overvoltage of the cathodic reaction, as shown in Figure 6.1. Hence, the hydrogen evolution rate for AM60B-MP was less than that of either AZ31B-MP or AM30-MP for the open circuit condition. It is consistent with the extrapolated i_{corr}, which indicates the AM60B-MP exhibited a lower corrosion rate than AZ31B-MP and AM30-MP.

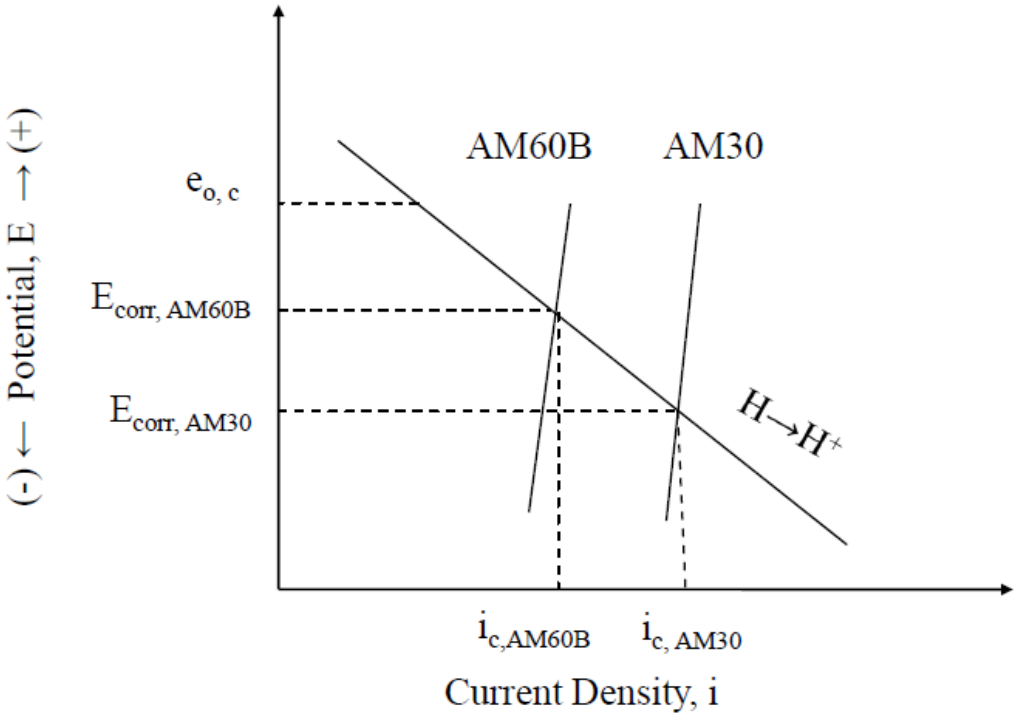

Figure 6.1 Reduced cathodic polarization occurs on AM60B due to the more positive E_{corr}.

In contrast to the cathodic process, charge transfer for the anodic reaction occurs at the interface between the metal surface and surface film. It was observed that the anodic Tafel slopes from the anodic polarization curves 100 mV below E_b for all the alloys were remarkably high but did not tend to infinity (Figure 5.8). This provides direct evidence that the anodic dissolution process was not activation controlled, but was mass transport controlled. For activation controlled kinetics, anodic dissolution activity is related to the electrochemical properties of the base metal. According to the Electromotive Force (emf) Series, Al and Zn are electrochemically more noble than Mg. Song et al [24] experimentally confirmed that the Al-rich β-phase had a more noble E_{corr} than the α-Mg matrix. These chemical composition and microstructure variables will certainly have a

strong influence on the anodic dissolution reaction. For mass transport controlled kinetics, there are two steps: mass diffusion through the surface film and through the electrochemical double layer between the solution and surface film [68]. Baril et al [4] experimentally confirmed that the influence of solution agitation on the polarization behaviour of pure Mg was negligible, which indicated that mass transport from the surface to the solution did not play a major role in controlling the overall mass transport process. However, it has be shown that limited ionic mobility in the passive film restricts the mass transport process of Mg^{2+} through the surface film [49]. Thus, the chemistry and structure of the surface film could be critical factors influencing the overall mass transport process and consequently affecting the anodic dissolution rate of the Mg-Al alloys. Understanding the influence of the bulk material and environment on the electrochemical process through the film will be of great help in understanding the corrosion resistance of Mg-Al alloys in the partially passive state. Furthermore, the corrosion behaviour of Mg alloys at potentials 100 mV below E_b is controlled by the anodic half-cell reaction rather than cathodic half-cell reaction. This is consistent with the reported literature [4, 49].

The improved corrosion resistance of AM60B-MP at the applied potential of –100 mV versus E_b (Figure 5.9) is due to the improved surface film. Nordlien *et. al* [15] reported that increasing the alloy Al content could increase the Al content of the surface film. Due to the n-type semiconductor property of the surface film, a higher-valence addition (Al^{3+})

can decrease Mg^{2+} diffusivity [68] and consequently improve the corrosion resistance of the Mg alloy by reduced mass transport.

Song et al [24] reported that the presence of 1 wt % Zn in the α-Mg matrix did not affect the protective properties of the surface film. In this study, a comparison of the corrosion kinetic parameters (Table 5.3) and the potentiostatic plot (Figure 5.9) for AZ31B-MP and AM30-MP confirmed that the addition of 1 wt % Zn did not have a significant influence on the corrosion resistance of Mg-Al alloys at an open circuit potential below E_b.

The E_{corr} for the dual-phase AM60B-MP was measured to be approximately 160 mV more noble versus AZ31B-MP and AM30-MP (Table 5.3). This result was consistent with the widely accepted theory that increased alloy Al content increases E_{corr} [24, 56-58]. However, all of the Mg-Al alloys exhibited a similar E_b (Table 5.3). As a consequence, the more positive E_{corr} exhibited by AM60B-MP reduced the difference between E_{corr} and E_b and increased the risk of localized corrosion. This finding leads to a redefinition of the role played by Al which has two opposite effects on Mg alloy corrosion resistance at potentials below E_b, which in the present case is a reduction in the anodic dissolution rate while increasing the risk of localized corrosion. Thus, AM60B-MP exhibited a lower corrosion rate than AZ31B-MP and AM30-MP, but likely has more of a risk of localized corrosion.

6.1.2 Corrosion Behaviour Above E_b

At the applied potential +100 mV versus E_b, the steady-state anodic current density transient was at least one order of magnitude higher than that recorded at –100 mV versus E_b (Figure 5.9). Considering the observed pit-like localized corrosion attack (Figure 5.11) and observed rough corrosion surface (Figure 5.10), it is indicated that the surface film broke down at some weak sites and caused a dramatic increase in the anodic current density due to localized corrosion occurring on film-free areas.

In this study, the observed E_b exhibited by all of the MFERD alloys in room temperature GM9540P solution was similar (Table 5.3). This suggests that a common factor controlled the surface film breakdown process. Possible factors could be second phases [42-43, 57-59], the chemical composition of the α-Mg matrix [5], aggressive anions in the solution (in this case Cl^-) [19-20, 69] or the composition and microstructure of the surface film [42].

It has been reported that second phases in Mg-Al alloys could be effective micro-cathodes between the second phases and the α-Mg matrix [42-44, 58-59]. This micro-galvanic activity could drive localized passivity breakdown at flaws in the surface film adjacent to the second phase. However, in this study, the observed randomly distributed and relatively deep pits on either dual phase alloy, AM60B (Figure 5.11), or single phase alloys, AM30 (Figure 5.5) and AZ31B (Figure 5.11), indicate that AM60B-MP did not exhibit preferential corrosion attack of the α-Mg matrix at potentials +100 mV versus E_b

(Figure 5.11). Both single phase Mg-Al alloys (AZ31B-MP and AM30-MP: α-Mg) and the dual phase alloy (AM60B-MP: α-Mg + β-$Mg_{17}Al_{12}$) exhibited comparable E_b (Table 5.3). This indicates that the presence of β-phase did not strongly affect passive film breakdown. In addition, there was no preferential corrosion attack around the Al-Mn intermetallic particles from either corroded surfaces (Figure 5.4 and Figure 5.10) or from the cross-sectional views of the corroded surfaces (Figure 5.5 and Figure 5.11). This suggests that the Al-Mn intermetallics did not have a strong influence on the passive film breakdown process. This latter observation agrees with the work of Merino et al [31], who found that Al-Mn particles only affected the initial stages of passive film breakdown. In addition, the same E_b measurement for all the Mg alloys suggests that 1wt % Zn did not strongly affect the surface film breakdown process since it was only present in AZ31B-MP.

From the above discussion, it can be concluded that the described compositional factors – e.g β-phase, Al-Mn intermetallics, solute Zn or Al in the α-Mg matrix – did not affect the passive film breakdown. The presence of an aggressive anion in solution, such as Cl^-, however, may play a critical role in the breakdown of the surface film.

When the anodic potential is increased, anions in the solution, such as Cl^-, OH^-, or HCO_3^-, will be adsorbed onto the surface. As a result, anion migration may be a critical factor controlling surface film formation and breakdown. Cl^- can penetrate into the film through defect sites to react with metal cations at the metal/film interface to form

magnesium-hydroxyl-chloride compounds [13]. It is also known that the CO_3^{2-} ion is effective in retarding Mg dissolution by inhibiting mass diffusion from the metal/oxide interface to the oxide/solution interface due to the formation of an insoluble $Mg(OH)_2$-$MgCO_3$ layer [15, 18]. This suggests that Cl^-, HCO_3^- and OH^- will compete with each other for adsorption on the oxide surface, which is in turn, is dependent on their concentration in the solution. In this study, the same Cl^- containing solution (GM9540P) was used for all tests, thereby, providing a common electrochemical environment for the surface film breakdown process. According to the stress-rupture film breakdown mechanism [5, 61, 70], growth of Cl^- containing particles can generate osmotic stresses at the metal/oxide interface and in the barrier layer because their Pilling-Bedworth ratio is greater than 1. Thus, continuing film growth leads to local fracture of the barrier layer [13, 31, 61]. The growth of the surface film was interrupted by film breakdown when the applied potential reached E_b [5].

Based on the anodic cyclic polarization curves (Figure 5.8(c)), all MP surfaces exhibited a similar anodic branch above E_b. This indicates that all of the alloys exhibited similar anodic polarization behaviour after surface film breakdown. In addition, the steady-state current densities exhibited by all MP surfaces at an applied potential +100 mV versus E_b (Figure 5.9) were within a factor of two of each other. The differences in current densities can not be confirmed to be significant for this experiment due to the experimental error of one measurement. Comparison with the cyclic polarization curves shows that the anodic branch for all MP surfaces overlaps each other above E_b. This gives confidence that these

differences in anodic current densities are much smaller in comparison with those below E_b. This implies that the presence of the semi-continuous β-phase network in AM60B-MP did not provide significant micro-galvanic activity to drive anodic dissolution of the α-Mg matrix. This agrees well with the claim of Lunder et al. [44]. Thus, the presence of β-phase may not have significant influence on the anodic dissolution kinetics of the α-Mg matrix. Deep localized corrosion attack was observed on the AM60B-MP surface (Figure 5.11) which indicates that the semi-continuous β-phase network was not sufficient to prevent corrosion attack of the α-Mg matrix. Since the anodic dissolution rate of α-Mg is much faster than that of β-phase [44], the overall anodic corrosion process would be dominated by the anodic dissolution of the α-Mg matrix at areas of film breakdown. The similar chemical composition of the α-Mg matrix for all the experimental alloys would lead to the expectation that they would have a similar anodic current density at potentials above E_b. However, AM60B-AR exhibited a higher anodic current density at +100mV versus E_b than all MP surfaces. This may be due to contamination on the surface from the alloy fabrication.

6.1.3 Skin Effect

The skin thickness of die-cast Mg-Al alloys was defined using micro-hardness profiles across the casting skin thickness and/or by changes in grain size [37, 40]. Micro-hardness profiles across the casting thickness of the experimental AM60B (Figure 4.7) shows that there was a harder skin layer approximately 200 μm thick. Figure 4.7 shows that the microstructure of the die-cast AM60B gradually changed from a surface skin layer which

contained finer grains and a higher fraction of β-phase precipitates along the grain boundaries to the interior which consisted of larger grains and lower fractions of β-phase. Due to the better corrosion resistance of the β-phase, the skin of die-cast Mg alloys usually exhibits better corrosion resistance than its interior. This is known as the skin effect [21]. In contrast with die-cast AM60B, extruded AM30 did not show a micro-hardness difference between its skin and interior (Figure 4.7). However, the extruded AM30 had a surface layer that was approximately 200 μm thick containing coarser grains compared with those of the interior. The difference between the corrosion properties of the skin and interior for both of these alloys have been evaluated in this study.

In Figure 5.8(b), significantly different anodic polarization behaviour between the mechanical polished (MP) surface (i.e. interior) and the as-received (AR) (i.e. skin) surface of AM60B was observed at potentials below E_b, namely that the AM60B-AR exhibited lower anodic current density and higher E_{corr} than AM60B-MP. This observation agrees well with the study of Song et al [21, 39]. This can be explained by Figure 6.2 which shows that the reduction of i_{corr} can be attributed to the increased E_{corr}. Having approximately the same steady-state cathodic current density recorded for both AM60B-MP and AM60B-AR (Figure 5.14) suggests that the corrosion process is controlled by the anodic reaction. This is consistent with the discussion in section 6.1.1. The improved corrosion resistance could arise from an improved surface film formed on the higher fraction of the Al-rich β-phase in the casting skin structure. To a large extent, the mass transport process of Mg cations could be reduced by this enhanced surface film.

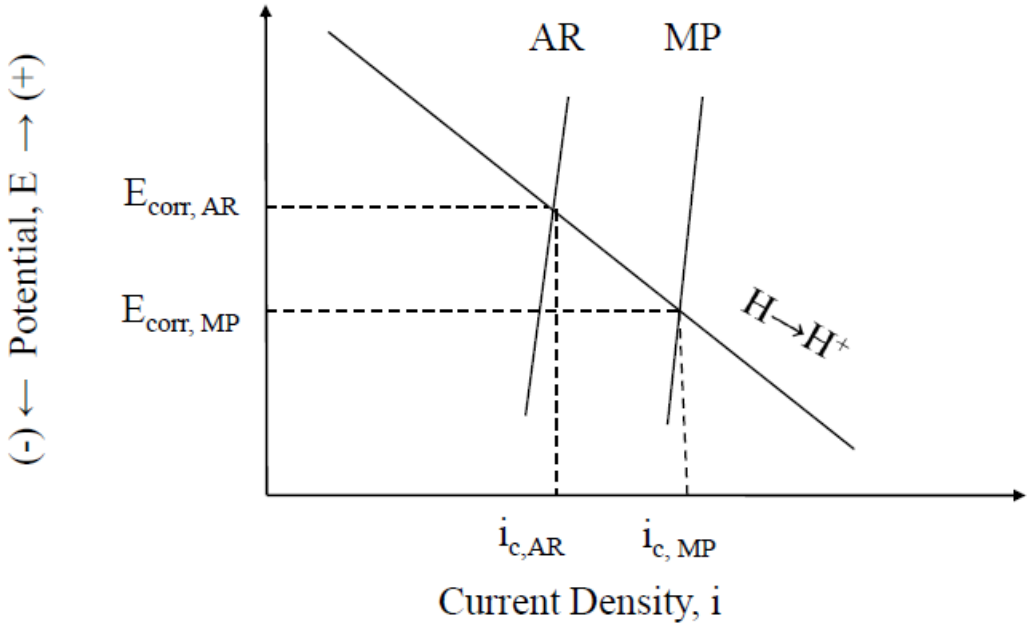

Figure 6.2 Illustration of the reduced i_{corr} of AM60B skin (AR) due to the more noble E_{corr}.

Both the AM60B-AR and AM60B-MP surfaces exhibited similar E_b, whereas the E_{corr} measured for the AM60B-AR surface was approximately 40 mV more positive than that measured for the AM60B-MP surface (Table 5.3). The difference between E_{corr} and E_b was lowest for AM60B-AR. This means that AM60B-AR can only withstand small changes in anodic polarization without initiating breakdown of the stable surface film. For this reason, the skin of AM60B is more susceptible to localized corrosion than its interior. The similar E_b of AM60B-MP and AM60B-AR provides more evidence to support that the fraction and continuity of the β-phase had no significant influence on the

surface film breakdown process. On the other hand, the high fraction and improved continuity of the β-phase in the die-cast skin could form an additional barrier layer to reduce the mass transport rate of Mg cations through the surface film, and consequently reduce the corrosion rate of Mg-based alloys.

However, at an applied potential 100 mV above E_b, the pit-like localized corrosion observed on both the AM60B-MP and AM60B-AR surfaces did not show significant differences in depth (less than 50 μm), as shown in Figure 5.11. Pits tended to propagate over the surface instead of penetrating deeper into the alloy. There was no preferential dissolution of the α-matrix observed on either the AM60-AR or AM60-MP surfaces. This agrees well with the findings of Lunder et al [44], who stated that the presence of β-phase does not cause micro-galvanic corrosion. In addition, similar anodic polarization branches above E_b and the order of magnitude agreement between the steady state current density recorded at an applied potential +100 mV versus E_b for AM60B-MP and AM60B-AR (Figure 5.9) imply that the relative fractions of β-phase had no significant influence on the anodic dissolution kinetics. Due to the lower anodic dissolution rate of β-phase [24, 27, 44], anodic dissolution of the α-Mg matrix may dominate the localized corrosion at surface film breakdown areas.

In contrast with the die-cast AM60B fine grained two-phase skin layer, the extruded AM30 contained coarse, single phase α-Mg grains in the skin layer (Figure 4.4). However, this microstructural difference did not have a significant effect on the AM30

potentiodynamic polarization behaviour in the GM9540P solution at room temperature, as shown by the similar cathodic and anodic branches (Figure 5.8 (a)) and insignificantly different kinetic parameters (Table 5.3). This confirms that grain size does not have a significant influence on the corrosion resistance of single phase α-Mg alloys. The role of grain size in the two-phase microstructure affects the continuity of the β-phase network and the fraction of β-phase.

6.1.4 Influence of Crystallographic Orientation

The extruded AM30 showed a slightly stronger {0002} texture on the TT-TD plane than that exhibited on the other planes, ED-TT and ED-TD (Figure 5.1). However, no significant difference in either the cathodic or anodic polarization behaviour was observed between each sample plane either in the GM9540P solution after short term pre-exposure (Figure 5.2) or in the 0.01 M NaCl solution after long term pre-exposure (Figure 5.6). For the same corrosion conditions, all planes corroded at the same E_{corr} with the same i_{corr}, as shown in Table 5.1, Table 5.2 and Figure 5.7. Also, the steady-state anodic current densities at the applied potential 100 mV below E_b and above E_b were not significantly different (Figure 5.3). This confirmed that the observed weak crystallographic texture of the extruded AM30 did not have a significant influence on the anodic corrosion behaviour.

Song et al [26] claimed that a 10% mixture of basal and prism planes will reduce the difference of anodic dissolution rate from a factor of 20 to 6.5. The more random the

crystallographic texture, the lower the differences in anodic dissolution rate. The theoretically calculated dissimilar electrochemical performance between the basal and prism planes [26] provides a possible driving force for micro-galvanic corrosion. However, the cross-sectional view of the corroded surface (Figure 5.5) shows that all sample planes exhibited the same corrosion resistance at the applied potential both 100mV below and above E_b. There was no preferential corrosion attack observed for any particular grains. At the potential 100mV above E_b, pit-like localized corrosion occurred on multiple grains and tended to propagate. This suggests that no significant micro-galvanic corrosion occurred by the coupling of differently oriented grains of α-Mg.

6.1.5 Influence of Aging on Corrosion Behaviour

The long-term corrosion resistance of extruded AM30 on each sample plane was investigated in a 0.01 M NaCl solution. In general, the corrosion behaviour observed on the extruded AM30 planes follows the same trend with increasing aging time. After both short-term and long-term pre-exposure, the potentiodynamic polarization curves (Figure 5.6) showed an apparently positive E_b relative to E_{corr} for all three planes. This indicates that AM30 was in a partially protected state by a surface film at the open circuit potential for 7 days in room temperature 0.01 M NaCl.

A comparison of the extrapolated cathodic kinetic parameters (Table 5.2) from the potentiodynamic polarization curves after short-term and long-term pre-exposure showed that the cathodic Tafel slope and $i_{o,c}$ did not change significantly with increasing pre-

exposure time. This suggests that the cathodic kinetics were independent of aging time. Considering that $i_{o,c}$ is highly sensitive to surface condition, the top layer of the surface film, where the hydrogen evolution occurred, underwent no significant change in chemical composition and microstructure during immersion. This is consistent with the discussion of the cathodic reaction in section 6.1.1 and agrees well with reported surface film analyses in mildly aggressive solutions, in which the top layer of the surface film formed is mainly $Mg(OH)_2$-$MgCO_3$ [15, 18].

In this study, the more positive E_{corr} and E_b measured after long-term pre-exposure (in Table 5.2) aggress well with the study by Hara et al [5]. They observed that the surface film became thicker with increasing pre-exposure time and caused an increase in E_{corr} and E_b due to the surface film resistance increasing with film thickness [51], thereby retarding mass transport through the film and slowing anodic dissolution. The extrapolated current density from potentiodynamic polarization curves after one hour pre-exposure is over one order of magnitude higher than that after long term pre-exposure (Table 5.2). This result is also consistent with the reported decrease of anodic current density at potentials below E_b with increasing film thickness [5]. For this reason, it establishes the enhanced barrier effect of the passive surface film by increasing immersion time in dilute solutions. During long time immersion, both potentiodynamic polarization tests (Table 5.2) and LPR tests (Figure 5.7) showed approximately constant E_{corr} and corrosion rate. This suggests that the AM30 exhibited a steady-state corrosion condition in the 0.01 M NaCl solution at the

open circuit potential. This may be attributed to the relatively stable surface film formed on the exposed surface which provides a stable protective barrier for the substrate.

Chapter 7. Conclusions

From the foregoing study on the corrosion resistance of three of the MFERD alloys (AZ31B, AM30 and AM60B) in a near-neutral saline solution, the following conclusions can be drawn:

1. Partially protective surface films can be formed on AZ31B, AM60B and AM30 in a near-neutral mildly aggressive saline solution (GM9540P).
2. The similar breakdown potentials (E_b) measured for all alloys indicates that metallurgical factors, such as the bulk chemical composition, the presence of β-phase ($Mg_{17}Al_{12}$) and intermetallic particles do not have a significant influence on the surface film breakdown process.
3. At 100mV below E_b, the apparent relative ranking of corrosion resistance is given by: AM60B > AM30≈ AZ31B. By contrast, at 100 mV above E_b, the differences of anodic dissolution rates are too small to apply a relative ranking between these alloys.
4. Increasing the alloy Al content has two opposing effects on the corrosion resistance of Mg alloys: it can improve the corrosion resistance of the film to reduce the corrosion rate and increase the corrosion potential (E_{corr}), but the smaller difference between the E_{corr} and E_b increases the risk of localized corrosion.

5. An alloying addition of 1 wt % Zn does not have a significant influence on the corrosion resistance of Mg-Al alloys.
6. A semi-continuous β-phase ($Mg_{17}Al_{12}$) grain boundary network does not provide sufficiently strong micro-galvanic activity to significantly influence the corrosion resistance of Mg-Al alloys.
7. The die-cast skin of AM60B only exhibits better corrosion resistance versus its interior before the breakdown of the film.
8. Long term pre-exposure in 0.01 M NaCl solution improves the corrosion resistance of Mg-Al alloys because the thicker film formed on the surface decreases the mass transport process and consequently reduce the anodic dissolution rate.

References

1. Cole, G., *Summary of Magnesium Vision 2020: A North American Automotive Strategic Vision for Magnesium*, in *Magnesium Technology 2007*, R.S.B.e. al, Editor. 2007, TMS 2007: Warrendale, PA. p. 35-40.
2. Alan A. Luo, E.A.N., Kumar Sadayappan, and Wenfang Shi, *A Canada-China-USA Collaborative Research and Development Project: Magnesium Front End Research and Development* 2008 Annual Progress Report. 2008, Niagara-on-the-Lake, Canada: Project Technical Committee.
3. Jönsson, M., D. Persson, and D. Thierry, *Corrosion product formation during NaCl induced atmospheric corrosion of magnesium alloy AZ91D.* Corrosion Science, 2007. **49**(3): p. 1540-1558.
4. Baril, G. and N. Pébère, *The corrosion of pure magnesium in aerated and deaerated sodium sulphate solutions.* Corrosion Science, 2001. **43**(3): p. 471-484.
5. Hara, N., et al., *Formation and breakdown of surface films on magnesium and its alloys in aqueous solutions.* Corrosion Science, 2007. **49**(1): p. 166-175.
6. Ghali, E., W. Dietzel, and K.-U. Kainer, *General and localized corrosion of magnesium alloys: A critical review.* Journal of Materials Engineering and Performance, 2004. **13**(1): p. 7-23.
7. Lindström, R., et al., *Corrosion of magnesium in humid air.* Corrosion Science, 2004. **46**(5): p. 1141-1158.
8. Brun, C.H., J. Pagetti, and J. Talbot, *Investigation of the Corrosion of Magnesium in Aqueous Solutions of 3 wt % Sodium Chloride at Room Temperature.* Memoires Scientifiques de la Revue de Metallurgie, 1976. **73**(10): p. 659-668.
9. Feliu Jr, S., et al., *Atmospheric corrosion of magnesium alloys AZ31 and AZ61 under continuous condensation conditions.* Corrosion Science, 2011. **53**(5): p. 1865-1872.
10. Feliu Jr, S., et al., *Effect of naturally formed oxide films and other variables in the early stages of Mg-alloy corrosion in NaCl solution.* Electrochimica Acta, 2011. **56**(12): p. 4554-4565.
11. Feliu Jr, S., et al., *Correlation between the surface chemistry and the atmospheric corrosion of AZ31, AZ80 and AZ91D magnesium alloys.* Applied Surface Science, 2009. **255**(7): p. 4102-4108.
12. Lin, C. and X. Li, *Role of CO_2 in the initial stage of atmospheric corrosion of AZ91 magnesium alloy in the presence of NaCl.* Rare Metals, 2006. **25**(2): p. 190-196.
13. Lindström, R., L.G. Johansson, and J.E. Svensson, *The influence of NaCl and CO2 on the atmospheric corrosion of magnesium alloy AZ91.* Materials and Corrosion, 2003. **54**(8): p. 587-594.
14. Makar, G.L. and J. Kruger, *Corrosion of magnesium.* International Materials Reviews, 1993. **38**(3): p. 138-153.

15. Nordlien, J.H., et al., *Morphology and Structure of Oxide Films Formed on MgAl Alloys by Exposure to Air and Water*. Journal of the Electrochemical Society, 1996. **143**(8): p. 2564-2572.
16. Nordlien, J.H., et al., *A TEM investigation of naturally formed oxide films on pure magnesium.* Corrosion Science, 1997. **39**(8): p. 1397-1414.
17. Santamaria, M., et al., *Initial surface film on magnesium metal: A characterization by X-ray photoelectron spectroscopy (XPS) and photocurrent spectroscopy (PCS).* Electrochimica Acta, 2007. **53**(3): p. 1314-1324.
18. Wang, L., T. Shinohara, and B.-P. Zhang, *XPS study of the surface chemistry on AZ31 and AZ91 magnesium alloys in dilute NaCl solution.* Applied Surface Science, 2010. **256**(20): p. 5807-5812.
19. Wang, L., T. Shinohara, and B.P. Zhang, *Influence of chloride, sulfate and bicarbonate anions on the corrosion behavior of AZ31 magnesium alloy.* Journal of Alloys and Compounds, 2010. **496**(1-2): p. 500-507.
20. Wang, L., et al., *Characterization of surface products on AZ31 magnesium alloy in dilute NaCl solution.* Journal of Alloys and Compounds, 2009. **485**(1-2): p. 747-752.
21. Song, G., A. Atrens, and M. Dargusch, *Influence of microstructure on the corrosion of diecast AZ91D.* Corrosion Science, 1998. **41**(2): p. 249-273.
22. Song, G., et al., *The anodic dissolution of magnesium in chloride and sulphate solutions.* Corrosion Science, 1997. **39**(10–11): p. 1981-2004.
23. Song, G., et al., *The electrochemical corrosion of pure magnesium in 1 N NaCl.* Corrosion Science, 1997. **39**(5): p. 855-875.
24. Song, G., et al., *Corrosion behaviour of AZ21, AZ501 and AZ91 in sodium chloride.* Corrosion Science, 1998. **40**(10): p. 1769-1791.
25. Song, G., A.L. Bowles, and D.H. StJohn, *Corrosion resistance of aged die cast magnesium alloy AZ91D.* Materials Science and Engineering: A, 2004. **366**(1): p. 74-86.
26. Song, G.-L., R. Mishra, and Z. Xu, *Crystallographic orientation and electrochemical activity of AZ31 Mg alloy.* Electrochemistry Communications, 2010. **12**(8): p. 1009-1012.
27. Zhao, M.-C., et al., *Influence of the β-phase morphology on the corrosion of the Mg alloy AZ91.* Corrosion Science, 2008. **50**(7): p. 1939-1953.
28. Zhao, M.-C., et al., *Influence of pH and chloride ion concentration on the corrosion of Mg alloy ZE41.* Corrosion Science, 2008. **50**(11): p. 3168-3178.
29. Zhao, M.-C., et al., *An exploratory study of the corrosion of Mg alloys during interrupted salt spray testing.* Corrosion Science, 2009. **51**(6): p. 1277-1292.
30. Zhou, R.A.N.N.A.W., *Studies on the influence of chloride ion and pH on the corrosion and electrochemical behaviour of AZ91D magnesium alloy.* Journal of Applied Electrochemistry (July 2000), 2000. **30**(7): p. 865-874
31. Merino, M.C., et al., *Influence of chloride ion concentration and temperature on the corrosion of Mg–Al alloys in salt fog.* Corrosion Science, 2010. **52**(5): p. 1696-1704.

32. ASTM-Standard B275-05, *Standard Practice for Codification of Certain Nonferrous Metals and Alloys, Cast and Wrought*, ASTM International, West Conshohocken, PA, 2005.
33. Luo, A.A. and A.K. Sachdev, *Development of a New Wrought Magnesium-Aluminum-Manganese Alloy AM30.* Metallurgical and Materials Transactions A, 2007. **38**(6): p. 1184-1192.
34. Shaw, B.A., *Corrosion: Fundamentals, Testing, and Protection* ASM Handbook. Vol. 13A. 2003: ASM International.
35. Rafael Nunes, J.H.A., et.al, *Metallography and Microstructures* ASM-HANDBOOK. Vol. 2. 1992: ASM International.
36. Barbagallo, S., et al., *Divorced eutectic in a HPDC magnesium–aluminum alloy.* Journal of Alloys and Compounds, 2004. **378**(1-2): p. 226-232.
37. Weiler, J.P., et al., *Variability of skin thickness in an AM60B magnesium alloy die-casting.* Materials Science and Engineering: A, 2006. **419**(1-2): p. 297-305.
38. V.Baker, *Alloy Phase Diagrams*. ASM Handbook. Vol. 3. 1992: ASM International.
39. Aghion, E. and N. Lulu, *The effect of skin characteristics on the environmental behavior of die cast AZ91 magnesium alloy*. Journal of Materials Science, 2009. **44**(16): p. 4279-4285.
40. Shan, Z. and A.M. Gokhale, *Utility of micro-indentation technique for characterization of the constitutive behavior of skin and interior microstructures of die-cast magnesium alloys.* Materials Science and Engineering: A, 2003. **361**(1-2): p. 267-274.
41. Cheng, Y.-l., et al., *Comparison of corrosion behaviors of AZ31, AZ91, AM60 and ZK60 magnesium alloys.* Transactions of Nonferrous Metals Society of China, 2009. **19**(3): p. 517-524.
42. Pardo, A., et al., *Corrosion behaviour of magnesium/aluminium alloys in 3.5wt.% NaCl.* Corrosion Science, 2008. **50**(3): p. 823-834.
43. Zeng, R.-c., et al., *Review of studies on corrosion of magnesium alloys.* Transactions of Nonferrous Metals Society of China, 2006. **16**(Supplement 2): p. s763-s771.
44. O.Lunder, *The Role of $Mg_{17}Al_{12}$ Phase in the Corroison Mg Alloy AZ91*. Corrosion, 1987. **45**: p. 741-748.
45. Tunold, R., et al., *The corrosion of magnesium in aqueous solution containing chloride ions.* Corrosion Science, 1977. **17**(4): p. 353-365.
46. M.Pourbaix, *Atlas of Electrochemical Equilibria in Aqueous Solutions.* 1974: National Association of Corrosion Engineers.
47. Robert G. Kelly, J.R.S., David W. Shoesmith, Rudolph G.Buchheit, *Electrochemical Techniques in Corrosion Science and Engineering*. 2003, New york: Marcel Dekker, Inc.
48. Z, S.-S., *Mechanism of pit nucleation by electrical breakdown of the passive film.* Corrosion Science, 2002. **44**(5): p. 1143-1149.
49. Song, G.-L., *Corrosion of Magneisum Alloys*. 2011. 4.

50. Daloz, D., P. Steinmetz, and G. Michot, *Corrosion Behavior of Rapidly Solidified Magnesium-Aluminum-Zinc Alloys.* Corrosion, 1997. **53**(12): p. 944-954.
51. Heakal, F. and M. Fatayerji, *Electrochemical performance of Mg–9Al–1Zn alloy in aqueous medium.* Journal of Solid State Electrochemistry, 2011. **15**(1): p. 125-138.
52. J.E. Hillis, K.N.R., *High Purity Magnesium AM60 Alloy: The Critical Contaminant Limits and the Salt Water Corrosion Performance.* SAE Technical Paper 860288, 1986.
53. R K Singh Raman, N.B., J Efthimiadis, *Corrosion of Mg alloy AZ91 - the role of microstructure.* Corrosion Engineering Science and Technology, 2004. **39**(4): p. 346-350.
54. Shi, Z., M. Liu, and A. Atrens, *Measurement of the corrosion rate of magnesium alloys using Tafel extrapolation.* Corrosion Science, 2010. **52**(2): p. 579-588.
55. Song, G. and A. Atrens, *Recent Insights into the Mechanism of Magnesium Corrosion and Research Suggestions.* Advanced Engineering Materials, 2007. **9**(3): p. 177-183.
56. Song, G.L., *Recent progress in corrosion and protection of magnesium alloys.* Advanced Engineering Materials, 2005. **7**(7): p. 563-586.
57. Song, G.L. and A. Atrens, *Corrosion Mechanisms of Magnesium Alloys.* Advanced Engineering Materials, 1999. **1**(1): p. 11-33.
58. Song, G.L. and A. Atrens, *Understanding magnesium corrosion - A framework for improved alloy performance.* Advanced Engineering Materials, 2003. **5**(12): p. 837-858.
59. Chen, J., et al., *In situ observation of pit initiation of passivated AZ91 magnesium alloy.* Corrosion Science, 2009. **51**(3): p. 477-484.
60. Allan Froats, T.K.A., David Hawke, *Corrosion.* ASM-HANDBOOK. Vol. 13. 1992: ASM International.
61. Marcus, P., V. Maurice, and H.H. Strehblow, *Localized corrosion (pitting): A model of passivity breakdown including the role of the oxide layer nanostructure.* Corrosion Science, 2008. **50**(9): p. 2698-2704.
62. Yao, H.B., Y. Li, and A.T.S. Wee, *An XPS investigation of the oxidation/corrosion of melt-spun Mg.* Applied Surface Science, 2000. **158**(1-2): p. 112-119.
63. Splinter, S.J. and N.S. McIntyre, *The initial interaction of water vapour with Mg-Al alloy surfaces at room temperature.* Surface Science, 1994. **314**(2): p. 157-171.
64. Lindstrom, R., J.-E. Svensson, and L.-G. Johansson, *The Influence of Carbon Dioxide on the Atmospheric Corrosion of Some Magnesium Alloys in the Presence of NaCl.* Journal of the Electrochemical Society, 2002. **149**(4): p. B103-B107.
65. Martin, H.J., M.F. Horstemeyer, and P.T. Wang, *Structure–property quantification of corrosion pitting under immersion and salt-spray environments on an extruded AZ61 magnesium alloy.* Corrosion Science, 2011. **53**(4): p. 1348-1361.
66. Evans, U.R., *The corrosion and oxidation of metals: Supplementary volume.* 1968, New York: St. Martin's Press.

67. He, B.B., *Two- Dimensional X-Ray Diffreaction*. 1954, Hoboken, New Jersey: John Wiley & Sons,Inc.
68. A.Jones, D., *Principles and Prevention of Corrosion*. 1996, Upper Saddle River, New York: Prentice Hall.
69. Szklarska-Smialowska, Z., *Mechanism of pit nucleation by electrical breakdown of the passive film.* Corrosion Science, 2002. **44**(5): p. 1143-1149.
70. Mattin, S.P. and G.T. Burstein, *Detailed resolution of microscopic depassivation events on stainless steel in chloride solution leading to pitting.* Philosophical Magazine Letters, 1997. **76**(5): p. 341-348.